
Azimuthal Asymmetries in Unpolarized Semi-Inclusive DIS

Wolfgang Käfer



Physikalisches Institut
Albert-Ludwigs-Universität Freiburg

Azimuthal Asymmetries in Unpolarized Semi-Inclusive DIS

Diplomarbeit

vorgelegt

von

Wolfgang Käfer

Physikalisches Institut
Albert-Ludwigs-Universität
Freiburg

März 2008

Contents

1	Introduction	1
2	Theoretical Motivation	3
2.1	Deep Inelastic Scattering	3
2.2	Parton Distribution Functions	5
2.2.1	Polarized Distribution Functions	5
2.2.2	Transverse Momentum Dependent Distribution Functions	5
2.3	Semi-Inclusive DIS	6
2.4	Fragmentation	7
2.5	Azimuthal Modulations in Unpolarized SIDIS	8
2.5.1	Cahn Effect	9
2.5.2	The SIDIS Cross Section for Unpolarized Lepton - Nucleon Scattering	10
2.5.3	Perturbative QCD Effects	12
2.5.4	Polarized SIDIS	13
3	The COMPASS Experiment	15
3.1	The Beam Line	15
3.2	The Spectrometer	15
3.2.1	The Polarized Target	17
3.2.2	The COMPASS Trigger System	17
3.2.3	Tracking Detectors	18
3.2.4	Particle Identification	18
3.3	Data Reconstruction	19

4	Data Selection	21
4.1	Event Selection	21
4.1.1	Data Quality	21
4.1.2	Kinematic Range	22
4.1.3	The Primary Vertex	22
4.1.4	Beam and Scattered Muon	22
4.2	Hadron Selection	25
4.3	Leading Hadron Selection	25
4.4	Particle Identification	27
5	Acceptance Correction and Determination of the ϕ_h Dependence	31
5.1	Data and MC	31
5.2	Resolution and Binning	32
5.3	The Acceptance Correction	34
5.4	The Acceptance of the COMPASS Spectrometer	35
5.5	Determination of the Moments of the Cross Section	36
6	Results	43
6.1	Dependence on Kinematic Variables	43
6.2	The $\cos \phi_h$ Moment - the Transverse Momentum of the Quarks	49
6.3	The $\cos 2\phi_h$ Moment - Comparison with Theory	51
6.4	Systematic Checks	51
7	Summary and Outlook	57
A	Appendix	59
A.1	The $\sin \phi_h$ moment	59
A.2	Tables	62
	References	74
B	Deutschsprachige Zusammenfassung	77

1. Introduction

Scattering experiments have been the most important tool to probe the structure of matter for almost a century. Since the discovery of the atomic nucleus in the famous Rutherford-Experiment via the scattering of α particles on gold foil, scattering experiments have provided new and often surprising insights.

Although the existence of a substructure was known before (because of the anomalous magnetic moment of proton and neutron), the first direct evidence for a substructure of the nucleon has been found at SLAC¹ in the 1960s. Although historically also known as partons, the constituents of nucleons turned out to be quarks, spin $1/2$ particles carrying fractions of the elementary electric charge e . With the formulation of QCD [1, 2] in 1973 and the subsequent discovery of gluons at DESY² in 1979, our current picture of the nucleon emerged. The nucleon is thought to consist of three valence quarks, held together by gluons. The gluons can further fluctuate into so-called sea quarks, quark-antiquark pairs which exist only on a very short timescale.

While it is well known that the valence quarks carry only about half the momentum of the nucleon, the situation concerning the nucleon spin is less clear. The total spin of the nucleon of $1/2$ was originally thought to be dominated by contributions of the spin of the valence quarks. However, this assumption was ruled out by measurements of the EMC³ experiment at CERN⁴ [3]. This was later confirmed by other experiments and today it is established that the contribution of the quark spin to the spin of the nucleon is only about 25%. Until today, it is not clear where the spin of the nucleon comes from.

Another rather unknown quantity are the transverse momenta of the quarks inside the nucleon. Since calculations are usually made in a boosted frame, where the nucleon carries high momentum, the momentum component of the quarks transversely to the boost direction is small and often neglected. On the other hand, the nucleon has a finite size, so the transverse momentum has to be non-zero already according to the uncertainty principle.

The investigation of azimuthal asymmetries in unpolarized semi-inclusive Deep Inelastic Scattering (DIS) was originally proposed by H. Georgi and H. D. Politzer as a clean test of perturbative QCD in [4]. However, it was pointed out by R. Cahn immediately afterwards [5] that azimuthal modulations can also be caused by the transverse momentum of the quarks, which is known as Cahn Effect. Azimuthal asymmetries have gained

¹Stanford Linear Accelerator Center

²Deutsches Elektronen SYnchrotron

³European Muon Collaboration

⁴European Organization of Nuclear Research

renewed interest with the attempt to parameterize the nucleon with transverse momentum dependent parton distribution functions starting in the 1990s [6]. Up to now, results on these asymmetries have been published by the EMC Collaboration in [7, 8], the E665 experiment at Fermilab in [9] and by the ZEUS Collaboration [10] at DESY. However, these results have been obtained in different kinematic regions and thus are difficult to compare. The concepts of DIS as well as the different effects contributing to azimuthal modulations observed in unpolarized semi-inclusive DIS are discussed in Chapter 2.

After a previous attempt [11], this thesis dedicated to the determination of these modulations from data taken at the COMPASS⁵ experiment at CERN. The data used in this thesis, were taken in 2004 with longitudinal (i.e. parallel to the beam axis) target polarization. An effort to extract the same modulations from data taken with transverse target polarization is also ongoing [12]. Since the experimental conditions differ for the two polarizations, this gives an opportunity to study systematic effects. The COMPASS experiment in the longitudinal setup is briefly described in Chapter 3. It is operating in a kinematic region similar to EMC, but has a much larger data sample and thus can measure the dependence on the kinematic variables more precisely.

The method used in this thesis to extract these modulations from COMPASS data is described in the following chapters. Chapter 4 gives a detailed description of the performed event selection. Since azimuthal modulations are also generated by the non-uniform acceptance of the COMPASS spectrometer, a Monte Carlo simulation is needed in order to correct for these effects. Chapter 5 characterizes the MC simulation performed for this task and describes how the measured angular distributions are corrected for acceptance effects and the moments of the modulations are determined. The obtained results will be discussed in Chapter 6 and an estimate of the transverse quark momentum based on the measured $\cos \phi_h$ moment of the cross section is given. Additionally, the measured $\cos 2\phi_h$ moment is compared with a recent model calculation, which estimates different contributions to this asymmetry.

⁵Common Muon Proton Apparatus for Structure and Spectroscopy

2. Theoretical Motivation

This chapter is dedicated to a brief introduction to the theoretical concepts needed in this thesis. It is organized as follows: After a very short introduction to Deep Inelastic Scattering in Sec. 2.1, parton distribution functions are described in Sec. 2.2. In Sec. 2.3, the DIS formalism is adapted to the Semi-Inclusive Deep Inelastic Scattering (SIDIS) process, where an additional hadron is observed in the final state. Finally in Sec. 2.5, several sources for modulations of the SIDIS cross section with the hadron azimuthal angle ϕ_h are discussed. This chapter is based mainly on [6, 13, 14]

2.1 Deep Inelastic Scattering

Deep inelastic scattering is used to gain information about the inner structure of composite particles like the nucleon. In a typical DIS reaction as depicted in Fig. 2.1 a lepton l scatters off a nucleon N to produce a hadronic final state X together with the scattered lepton l' :

$$l + P \rightarrow l' + X . \quad (2.1)$$

The term Deep Inelastic Scattering is used, when the 4-momentum transfer Q of the lepton to the hadron is large enough that the substructure of the nucleon can be re-

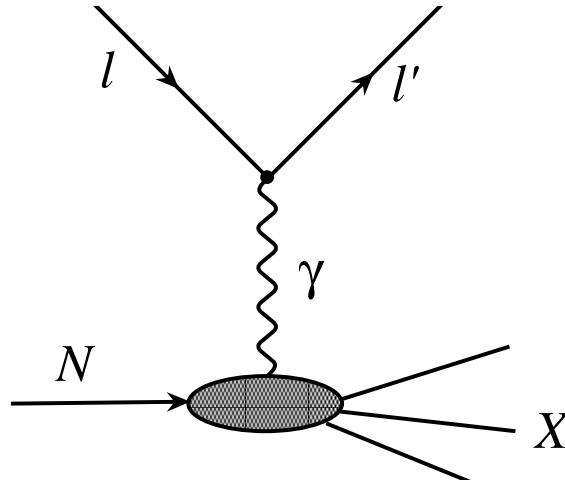


Figure 2.1: Schematic picture of the DIS process: A lepton l interacts with a Nucleon N via the exchange of a virtual photon γ . While the leptonic part of the interaction can be treated with perturbative QED, the hadronic part represented by the blob has to be parameterized with a priori unknown functions.

solved. In this case the timescale of the interaction $1/Q$ ($\hbar = c = 1$ in this thesis) is short. Thus the quarks in the nucleon do not interact with each other during the scattering reaction and the interaction can be seen as elastic scattering of leptons on free quarks. This can approximately be described in leading order QED with a one photon exchange between the lepton and one of the quarks of the nucleon. W/Z exchange is also possible but does not contribute at the COMPASS beam energy of about 160 GeV. The quark is emitted from the nucleon and both the quark and the nucleon remnant fragment into hadrons.

The process is characterized by several (Lorentz-invariant) kinematical variables as defined in Tbl. 2.1. Theoretical predictions are often made in the center of mass system of the virtual photon and the nucleon, the so-called Gamma-Nucleon System (GNS). This system has the advantage, that in the DIS regime both proton and photon carry high momentum, and therefore quark masses can be neglected. In the GNS, the Bjorken scaling variable x can be interpreted as the momentum fraction of the nucleon carried by the quark.

Table 2.1: Definition of Kinematic Variables relevant for the DIS Process

mass of the target nucleon	M_N
4-momentum of the incoming muon l	$l^\mu = (E, \vec{l})$
4-momentum of the target nucleon P	$P^\mu = (E_N, \vec{p}_N)$
4-momentum of the outgoing muon l'	$l'^\mu = (E', \vec{l}')$
4-momentum of the virtual photon q	$q = l - l'$
4-momentum of outgoing hadron P_h	$P_h^\mu = (E_h, \vec{P}_h)$
neg. squared invariant mass of the virtual photon Q^2	$Q^2 = -q^\mu q_\mu$
energy transfer to the target ν	$\nu = P^\mu q_\mu / M_N$
Bjorken scaling variable x	$x = \frac{Q^2}{2P^\mu q_\mu}$
fractional energy transfer of the virtual photon y	$y = \frac{P^\mu q_\mu}{l^\mu P_\mu}$
fraction z_h of the energy of the virtual photon carried by hadron h	$z_h = \frac{P_\mu P_h^\mu}{P^\mu q_\mu}$
transverse momentum of the hadron w.r.t. the virtual photon P_t^h	(not Lorentz-invariant)

The DIS cross section $d\sigma$ is proportional to the product of the leptonic tensor $L_{\mu\nu}$ and the hadronic tensor $W_{\mu\nu}$

$$d\sigma \propto L_{\mu\nu} W^{\mu\nu} . \quad (2.2)$$

While $L_{\mu\nu}$ can be calculated explicitly in QED $L_{\mu\nu} = 2(l_\mu l'_\nu + l'_\mu l_\nu - l \cdot l' g_{\mu\nu})$, $W_{\mu\nu}$ is unknown. Symmetry arguments can be applied to reduce the number of independent components of $W_{\mu\nu}$ from 16 down to two, the structure functions $F_1(x, Q^2)$ and $F_2(x, Q^2)$, see e.g. [13]. An additional structure function $F_3(x, Q^2)$ is present in neutrino - nucleon scattering due to the parity violation on the weak interaction. It is important to note that this parameterization is model independent and follows only from these

symmetry arguments. In the parton model, which will be discussed next, the structure functions are related to Parton Distribution Functions (PDFs).

2.2 Parton Distribution Functions

In the quark-parton model quarks are treated as massless non-interacting particles, the partons, and QCD effects are ignored. In this case the dependence of the structure functions on Q^2 vanishes. This is known as scaling. Taking into account QCD effects, scaling does no longer hold exactly, leading to the so-called scaling violation. Structure functions can be expressed in terms of parton distribution functions $f_q(x)$, which can be interpreted as the probability $f_q(x)dx$ of finding a quark of flavor q with momentum fraction between x and $x + dx$

$$F_1(x) = \sum_q e_q^2 f_q(x), \quad (2.3)$$

where e_q is the charge of the quark with flavor q . The sum runs over the contributing quarks flavors, usually $q = \{u, \bar{u}, d, \bar{d}, s, \bar{s}\}$. Additional quark distribution functions are introduced, when spin and transverse momentum effects are taken into account. These will be described in the following section.

In the quark-parton model, $F_1(x)$ and $F_2(x)$ are related via the Callan-Gross relation

$$F_2(x) = 2xF_1(x), \quad (2.4)$$

which also is only an approximation, as soon as QCD contributions are included.

2.2.1 Polarized Distribution Functions

Including spin effects but still implicitly integrating out transverse quark momentum, two additional PDFs are needed, the helicity function $g(x)$ and the transversity distribution function $h(x)$ (flavor indices will be suppressed in the following). $g(x)$ is the probability difference between finding a quark with its spin parallel to the nucleon and the probability to find a quark with its spin antiparallel to the nucleon spin inside a longitudinally polarized nucleon. $h(x)$ is defined similarly for a transversely polarized nucleon. While $g(x)$ is already measurable in inclusive DIS, $h(x)$ has to be measured in semi-inclusive reactions due to its symmetry properties [6]: $h(x)$ is a chiral odd object, which means that it changes sign under a parity transformation. Since QED is parity conserving, a chiral odd function has to be combined with another chiral-odd object in order to make the cross section parity even. This is e.g. possible in semi-inclusive DIS, where the other object is a chiral odd fragmentation function like the Collins fragmentation function introduced below or in polarized proton-proton collisions via Drell-Yan processes, where the transversity distribution function enters the process twice.

2.2.2 Transverse Momentum Dependent Distribution Functions

Additional PDFs appear, when the transverse momentum k_t of the quarks is taken into account. However, they are not measurable in inclusive reactions, only in semi-inclusive

reactions, again due to their symmetry properties. Also the PDFs introduced above gain an explicit k_t dependence. Of particular interest for unpolarized SIDIS is the Boer-Mulders function $h_1^\perp(x, k_t)$, which can be interpreted as the probability difference between the two spin states of a transversely polarized quark inside an unpolarized nucleon. More details about spin and transverse dependent PDFs can be found in [6].

2.3 Semi-Inclusive DIS

In semi-inclusive DIS (SIDIS), the detection of at least one hadron h is required in addition to the scattered lepton

$$l + N \rightarrow l' + h + X . \quad (2.5)$$

This provides additional information about the structure of the nucleon. Also the process is more complex, since free quarks cannot be observed, but fragment into hadrons. Moreover the fragmentation process takes place at a rather low energy scale, where perturbative QCD is not applicable. This requires additionally models for this fragmentation process. Usually it is assumed that that the scattering process and the fragmentation are independent of each other. This is referred to as factorization and has to be shown for each process. For the case of transverse momentum dependent SIDIS, factorization has only recently been proven in [15]. Thus the SIDIS cross section can be split into three parts (see also Fig. 2.2), namely:

- the probability of finding a quark with the longitudinal momentum fraction x and possibly spin and transverse momentum, parameterized with a PDF as described in Sec. 2.2.
- the cross section for photon-quark scattering $d\sigma^{lq \rightarrow l'q}$, calculated perturbatively with QED.
- the probability for the struck quark to fragment into the observed hadron h , described by fragmentation functions $D_q^h(z_h)$ which will be described in the following Sec. 2.4.

For example, considering the simplest case of unpolarized SIDIS neglecting k_t dependence, the cross section is of the form

$$d\sigma^{lp \rightarrow lhX} \propto \sum_q f_q(x) d\sigma^{lq \rightarrow l'q} D_q^h(z_h) . \quad (2.6)$$

From this expression, SIDIS structure functions can be defined by summing over all quark and antiquarks and integrating out internal degrees of freedom like quark transverse momentum respecting conservation laws, i.e.

$$F(x, Q^2, z_h, P_t^h) = x \sum_q \int d^2\vec{p}_t d^2\vec{k}_t \delta^{(2)}(\vec{p}_t - \vec{k}_t - \vec{P}_t^h/z_h) f_q(x, k_t^2) D_q^h(z_h, p_t^2) , \quad (2.7)$$

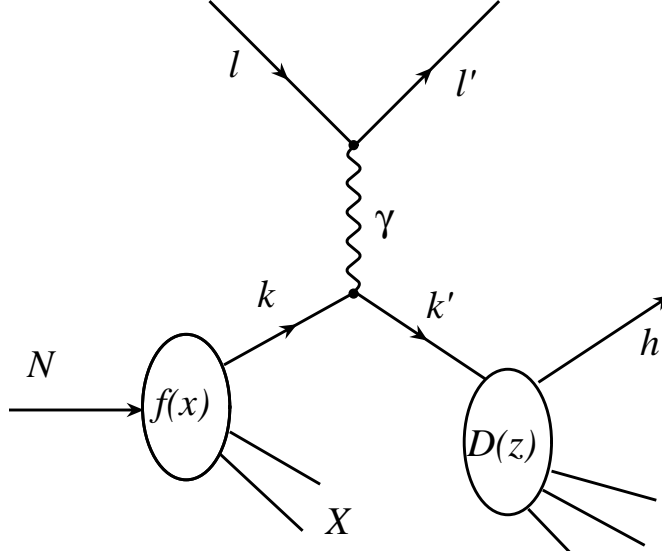


Figure 2.2: Schematic picture of the SIDIS process. The two blobs represent the two elements of the interaction which cannot be treated perturbatively: the internal structure of the nucleon described by a parton distribution function and the fragmentation process, parameterized with a fragmentation function.

where p_t is an additional transverse momentum of the hadron due to the fragmentation process. The full transverse momentum of the hadron is then given by:

$$\vec{P}_t^h = z_h \vec{k}_t + \vec{p}_t . \quad (2.8)$$

Further integration over the semi-inclusive variables z_h and P_t^h results in the well known DIS structure function $F_1(x, Q^2)$.

2.4 Fragmentation

The fragmentation process can be described similarly to the scattering process itself. While for the scattering process the soft parts are parameterized with PDFs, here the non perturbative parts are parameterized via fragmentation functions $D_q^h(z_h)$, which describe the process of hadronization. They can be interpreted as the probability for a quark of flavor q to produce a hadron h with energy fraction z_h . There is obviously a vast amount of possible combinations of quark flavors and hadron types. However, the number of independent fragmentation functions per hadron type can be significantly reduced with the assumption of isospin symmetry and charge conjugation invariance. Furthermore, one can distinguish the favored fragmentation function $D_{\text{fav}}(z_h)$, where the fragmenting quark enters the hadron as a valence quark, from unfavored ones $D_{\text{unf}}(z_h)$.

For the most common case, where the quark is an up or down quark fragmenting into a pion, one has:

$$D_{\text{fav}}(z_h) = D_u^{\pi^+}(z_h) = D_d^{\pi^-}(z_h) = D_{\bar{u}}^{\pi^-}(z_h) = D_{\bar{d}}^{\pi^+}(z_h), \quad (2.9)$$

$$D_{\text{unf}}(z_h) = D_d^{\pi^+}(z_h) = D_u^{\pi^-}(z_h) = D_{\bar{d}}^{\pi^-}(z_h) = D_{\bar{u}}^{\pi^+}(z_h). \quad (2.10)$$

If spin and transverse momentum effects are considered, additional fragmentation functions have to be introduced, similar to the additional PDFs. Worth mentioning here is the Collins fragmentation function $H_1(z_h)$, which gives the probability difference between the two polarization states for a transversely polarized quark to fragment into an unpolarized hadron.

2.5 Azimuthal Modulations in Unpolarized SIDIS

In leading order QED the cross section is independent of the hadron azimuthal angle ϕ_h , as long as transverse momentum effects are ignored. The azimuthal angle ϕ_h is defined as the angle between the lepton scattering plane spanned by incoming and scattered muon and the hadron production plane, which is spanned by virtual photon and hadron momentum (see Fig. 2.3). Thus ϕ_h can be calculated using the normal vectors of the two planes in terms of the momenta of the incoming muon \vec{l} , the virtual photon $\vec{q} = \vec{l} - \vec{l}'$ and the outgoing hadron \vec{P}_h via

$$\cos(\phi_h) = \frac{\vec{l} \times \vec{q} \cdot \vec{P}_h \times \vec{q}}{|\vec{l} \times \vec{q}| |\vec{P}_h \times \vec{q}|}. \quad (2.11)$$

The sign is defined as

$$\text{sign}(\phi_h) = \text{sign}[(\vec{q} \times \vec{l}) \cdot \vec{P}_h]. \quad (2.12)$$

Since ϕ_h is invariant both under a boost along the virtual photon axis and under spacial rotations, the above equations hold already in the lab frame.

Both k_t effects and QCD corrections introduce modulations of the cross section with respect to ϕ_h . As will be shown in the following the overall cross section measured at COMPASS is of the form

$$\frac{d\sigma}{d\phi_h} = a_0 + a_1 \cos \phi_h + a_2 \cos(2\phi_h) + a_3 \sin \phi_h. \quad (2.13)$$

where the two cosine terms receive contributions due to the Cahn Effect, perturbative QCD corrections and transverse momentum PDFs, while the sine term appears because of the polarized muon beam of the COMPASS experiment. In the following, sometimes the moments

$$\langle \cos(n\phi_h) \rangle = \frac{\int d\sigma \cos(n\phi_h)}{\int d\sigma} \quad (2.14)$$

of the cross section will be used. These can be obtained from the coefficients of Eq. 2.13 via

$$\langle \cos(n\phi_h) \rangle = \frac{a_n}{2a_0} \quad \text{for } n > 0. \quad (2.15)$$

and analogously for $\sin \phi_h$.

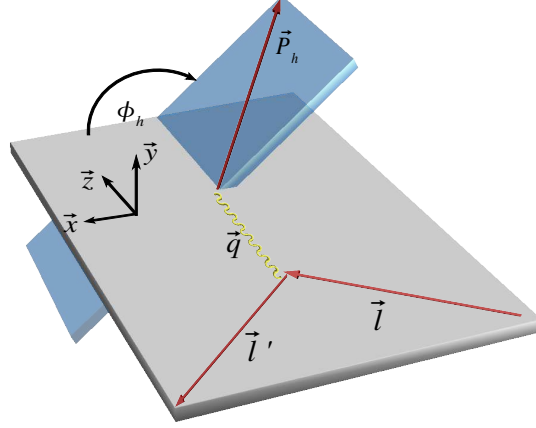


Figure 2.3: Definition of the hadron azimuthal angle ϕ_h . The coordinate system is chosen in such a way that the Z axis is along the direction of the virtual photon, the X axis lies in the lepton scattering plane along the remaining component of the scattered muon momentum and the Y axis is chosen such that the coordinate system is right handed.

2.5.1 Cahn Effect

As Cahn pointed out in [5], an azimuthal modulation of the cross section is already expected in leading order QED, when the transverse momentum of the quark is taken into account. The QED cross section is proportional to the squares of the Lorentz-invariant Mandelstam variables $s = (l + k)^2$ and $u = (k - l')^2$, where k denotes the 4-momentum of the scattered quark

$$d\sigma \propto s^2 + u^2. \quad (2.16)$$

Allowing for small transverse momentum $k_t \ll xP_h$, the quark 4-momentum k can be written as

$$k = (xP_h, k_t \cos \phi_q, k_t \sin \phi_q, xP_h). \quad (2.17)$$

ϕ_q is the azimuthal angle of the struck quark, which is not necessarily the same as the azimuthal angle of the hadron ϕ_h due to the additional transverse momentum p_t introduced in the fragmentation process. This leads to a smearing effect and thus diminishes the observed modulation [16]. Inserting Eq. 2.17 together with the lepton momentum

$$l = (E, l_x, 0, l_z) \quad (2.18)$$

in Eq. 2.16 leads to a dependence of the cross section on ϕ_q . Specifically, the result can be written as

$$\frac{d\sigma}{d\phi_q} \propto x^2(1 + (1 - y)^2) \left(1 - 2\frac{k_t}{Q} D_{\cos\phi_h}(y) \cos(\phi_q) + \left(\frac{k_t}{Q}\right)^2 D_{\cos 2\phi_h}(y) \cos 2\phi_q \right), \quad (2.19)$$

where the functions

$$D_{\cos\phi_h}(y) = \frac{(2 - y)\sqrt{1 - y}}{1 + (1 - y)^2} \quad (2.20)$$

and

$$D_{\cos 2\phi_h}(y) = \frac{(1 - y)}{1 + (1 - y)^2} \quad (2.21)$$

have been introduced.

The Cahn Effect is kinematically suppressed by $\frac{k_t}{Q}$ for $\cos(\phi_q)$ and $\left(\frac{k_t}{Q}\right)^2$ for the $\cos 2\phi_q$ term. These kinematic factors allow in principle to extract the mean transverse momentum of the quarks $\langle k_t \rangle$. When going from the quark to hadron level, the unpolarized PDFs and fragmentation functions need to be taken into account. Assuming Gaussian distributions for the transverse momentum dependence of $f_q(x, k_t)$ and $D_q^h(z_h, p_t)$,

$$f_q(x, k_t) = f_q(x) \frac{1}{\pi \langle k_t^2 \rangle} \exp\left(-\frac{k_t^2}{\langle k_t^2 \rangle}\right) \quad (2.22)$$

$$D_q^h(z_h, p_t) = D_q^h(z_h) \frac{1}{\pi \langle p_t^2 \rangle} \exp\left(-\frac{p_t^2}{\langle p_t^2 \rangle}\right), \quad (2.23)$$

a simplified cross section, neglecting the $\cos 2\phi_h$ term, can be written as [17]

$$\begin{aligned} \frac{d^5\sigma}{dx dy dz_h P_t^h dP_t^h d\phi_h} &\propto \sum_q \exp\left(-\frac{(P_t^h)^2}{\langle (P_t^h)^2 \rangle}\right) f_q(x) D_q^h(z_h) (1 + (1 - y^2)) \cdot \\ &\left[1 - 4D_{\cos\phi_h}(y) \frac{\langle k_t^2 \rangle z_h P_t^h}{Q \langle (P_t^h)^2 \rangle} \cos\phi_h \right]. \end{aligned} \quad (2.24)$$

The cosine moment defined in Eq. 2.14 can then be calculated using Eq. 2.15 to be

$$\langle \cos\phi_h \rangle = -2 \frac{D_{\cos\phi_h}(y) P_t^h z_h}{Q} \frac{\langle k_t^2 \rangle}{\langle (P_t^h)^2 \rangle}. \quad (2.25)$$

Thus in this simple model one expects a linear dependence of the cosine moment on z_h and P_t^h .

2.5.2 The SIDIS Cross Section for Unpolarized Lepton - Nucleon Scattering

If transverse momentum is no longer neglected, some of the symmetry arguments used to reduce the number of independent components of the hadronic tensor $W_{\mu\nu}$ are no

longer valid. Thus additional structure functions arise: The cross section for unpolarized SIDIS in terms of structure functions is given by [14]

$$\begin{aligned} \frac{d\sigma}{dx dy dz d\phi_h dP_t^h} = & \frac{\alpha^2}{xyQ^2} (1 + (1 - y)^2) \left(1 + \frac{\gamma^2}{2x}\right) \left(F_{UU} \right. \\ & \left. + D_{\cos \phi_h}(y) \cos \phi_h F_{UU}^{\cos \phi_h} + D_{\cos 2\phi_h}(y) \cos 2\phi_h F_{UU}^{\cos 2\phi_h} \right), \end{aligned} \quad (2.26)$$

with $\gamma = 2M_h \frac{x}{Q}$. The indices in F indicate beam and target polarization, or in this case the lack thereof (U = unpolarized). The dependence of the structure functions $F = F(x, Q^2, z_h, P_t^h)$ has been dropped here for simplicity. While there are several parameterizations for the cross section in terms of parton distribution functions, e.g. [14, 18, 19], Eq. 2.26 is model independent. As long as one stays in the pure parton-model, where QCD effects are switched off, it is possible to obtain an expression for the structure functions in terms of PDFs and fragmentation functions similar to Equation 2.7, see again [14]. As can be seen in Tbl. 2.2, the additionally involved PDFs and fragmentation functions in the unpolarized case are the transversity $h(x, k_t)$ and the Boer-Mulders function $h_1^\perp(x, k_t)$ introduced in Sec. 2.2, each combined with the Collins fragmentation function $H_1^\perp(z_h, p_t)$:

Table 2.2: PDFs and fragmentation functions contributing to the structure functions. The presence of the usual unpolarized PDF $f(x, k_t)$ and the corresponding fragmentation function $D(z_h, p_t)$ is due to the Cahn effect

Structure Function	contributing PDFs
F_{UU}	$f(x)D(z_h)$
$F_{UU}^{\cos \phi_h}$	$f(x, k_t)D(z_h, p_t), h_1^\perp(x, k_t)H_1^\perp(z_h, p_t), h(x, k_t)H_1^\perp(z_h, p_t)$
$F_{UU}^{\cos 2\phi_h}$	$f(x, k_t)D(z_h, p_t), h_1^\perp(x, k_t)H_1^\perp(z_h, p_t)$

Flavor and hadron type indices q, h have been dropped here. The contribution from transversity should be very small. $h(x)$ can be obtained from measurements performed by the HERMES collaboration with a proton target [20] and by the COMPASS collaboration on a transversely polarized Deuteron target [21]. The Collins fragmentation function needed to disentangle $h(x)$ and $H_1^\perp(z_h)$ can be determined from BELLE data [22]. These results lead to the conclusion that, although $h(x)$ is non-vanishing, for a deuteron target the up and down quark contributions to this combination cancel each other, because of the isospin symmetry of the deuteron [21].

Little is known of the Boer-Mulders function $h_1^\perp(x, k_t)$. A model calculation [23, 24] shows that the Boer-Mulders contribution to the $\cos 2\phi_h$ modulation might be of similar magnitude than the Cahn effect. However, due to the scarce experimental data, this model relies on rather strong assumptions. Predictions for COMPASS kinematics are available and will be compared to the results in Sec. 6.3. The Boer-Mulders Function may also contribute to the $\cos \phi_h$ asymmetry [14], but the size of this effect is unknown.

2.5.3 Perturbative QCD Effects

Perturbative QCD introduces a dependence on $\cos \phi_h$ already at order α_s . The relevant Feynman diagrams are shown in Fig. 2.4. The calculation of the cosine modulation has first been performed by H. Georgi and H. D. Politzer in 1977 [4] and has been discussed in detail in [25], on which this section is based. Recently, higher order contributions were calculated in [26]. At large z_h , the diagrams shown in 2.4 a) are dominant, since the gluons tend to fragment into softer quarks and thus the diagrams in b) can be neglected in the high z_h region. In this limit gluon bremsstrahlung predicts a $\cos \phi_h$ modulation with a negative amplitude. As $z_h \rightarrow 1$ the mean cosine moment of the cross section, defined in Eq. 2.14, can be approximated by

$$\langle \cos \phi_h \rangle \approx -\frac{\alpha_s}{2} \sqrt{1-z} D_{\cos}(y) . \quad (2.27)$$

The diagrams in b), where the observed hadron comes from the gluon, are most important in the low z_h region and give a positive amplitude, while the contribution from c) changes its sign at $z_h = 0.5$. The full expression can be found in the two publications mentioned above.

There is also a contribution to the $\cos 2\phi_h$ modulation, given in [27]. QCD effects are most important at $P_t^h > 1$ GeV [25, 17], so they are expected to be small for COMPASS kinematics, where most of the statistics is at low transverse momentum.

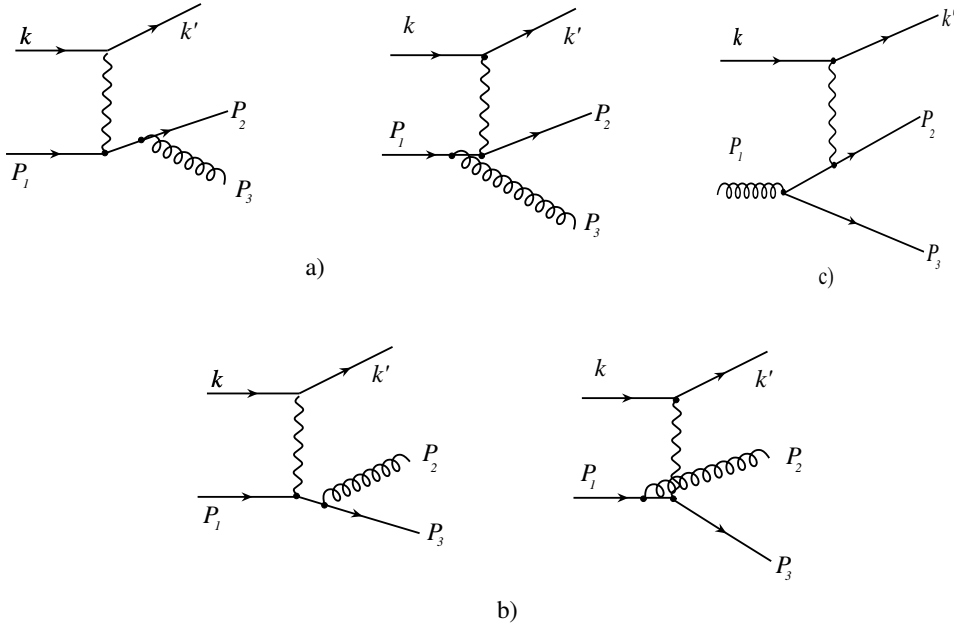


Figure 2.4: relevant Feynman diagrams for ϕ_h modulations at order α_s in SIDIS: In the diagrams in a), the observed hadron comes from the scattered quark, in b) from the bremsstrahlung gluon.

2.5.4 Polarized SIDIS

Since the muon beam used at the COMPASS experiment is naturally polarized, see Sec. 3.1, another angular modulation of the cross section is expected. In contrast to the Cahn and QCD contributions, the cross section for the beam asymmetry depends on $\sin \phi_h$ [14]. Therefore this effect can easily be separated from the Cahn and QCD contributions. Additional angular modulations arise, since COMPASS also measures with a polarized target (see Sec. 3.2.1). These cancel due to the combination of data taken with opposite polarization, therefore they are not discussed here. The cross section relevant for this thesis in terms of structure functions is thus:

$$\begin{aligned} \frac{d\sigma}{dx dy dz d\phi_h P_t^h dP_t^h} &= \frac{\alpha^2}{xyQ^2} (1 + (1-y)^2) \left(1 + \frac{\gamma^2}{2x}\right) \\ &\quad \left(F_{UU} + D_{\cos \phi_h}(y) \cos \phi_h F_{UU}^{\cos \phi_h} + D_{\cos 2\phi_h}(y) \cos 2\phi_h F_{UU}^{\cos 2\phi_h} \right. \\ &\quad \left. + D_{\sin \phi_h}(y) \sin \phi_h F_{LU}^{\sin \phi_h} \right), \end{aligned} \tag{2.28}$$

where $D_{\sin \phi_h}$ is given by

$$D_{\sin \phi_h} = \frac{y(1-y)}{1+(1-y)^2}. \tag{2.29}$$

Since the focus of the analysis lies on the two cosine modulations, the sine dependence will only be discussed in App. A.1.

3. The COMPASS Experiment

The COMPASS Experiment [28] was built to investigate the spin-structure of the nucleon. It is a fixed target experiment located at CERN. From 2002 to 2006¹ COMPASS measured with a naturally polarized μ^+ beam and a polarized Deuteron target. In 2007, COMPASS started taking data with a polarized liquid NH_3 target. For both cases, data was taken with the target longitudinally (i.e. along the beam axis) and transversely polarized. Since this thesis is based on data taken in 2004 with longitudinal target polarization, this chapter focuses on the setup in 2004 as depicted in Fig. 3.1.

3.1 The Beam Line

The COMPASS experiment is located at the end of the M2 beam line [29] of the SPS². It uses a secondary beam created with the SPS proton beam of 400 GeV scattering off a production target made of Beryllium. The beam is extracted from the SPS for 4.8 s, a so-called spill, followed by a break of 12 s. In one spill, about 10^{13} protons hit the production target, producing mainly pions and kaons. These subsequently decay into (anti)muons and neutrinos. The intensity of the final muon beam is about $3 \cdot 10^8$ muons/spill. With the exception of a short hadron run in 2004, COMPASS used a μ^+ beam with an energy of 160 GeV, which is naturally polarized due to the parity violation in the weak decay of the pions and kaons. The polarization is momentum dependent: Since the muon beam has a rather large momentum spread of 5% [28], a measurement of the momentum of each beam particle is required. This is done with the Beam Momentum Station (BMS), located about 100m in front (upstream) of the COMPASS target. Despite of several focusing magnets, the beam is accompanied by a rather large halo: the COMPASS target has a diameter of 3 cm, but the halo within 3 to 15 cm of the beam axis is still about 16% of the incoming flux, and about 7% of the muons are even further away. [28].

3.2 The Spectrometer

The COMPASS experiment consists of two stages, the Large Angle Spectrometer (LAS) and the Small Angle Spectrometer (SAS) to allow for precise momentum measurement starting from about 1 GeV up to about 100 GeV. Each stage has its own spectrometer magnet (SM1 and SM2). The COMPASS experiment features different types of tracking detectors, optimized for the required rates and resolutions and a hadronic calorimeter in each stage. The SAS also includes an electromagnetic calorimeter. A Ring Imaging Cherenkov detector (RICH) is included in the LAS, allowing separation of pions and kaons between 9 and 43 GeV.

¹apart from a break in 2005 because of the SPS upgrade for the LHC

²Super Proton Synchrotron

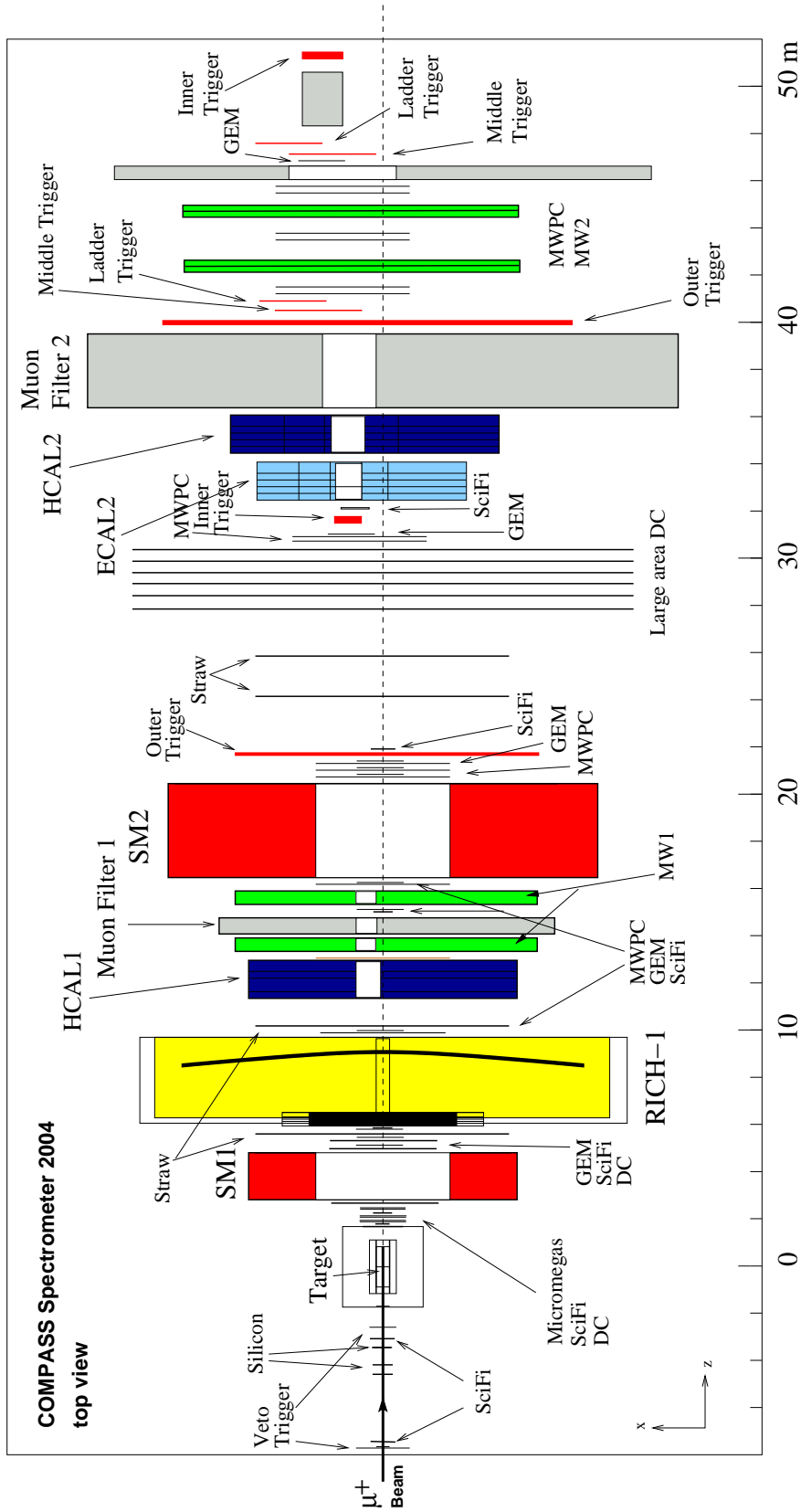


Figure 3.1: Schematic view of the COMPASS Spectrometer in 2004 [28].

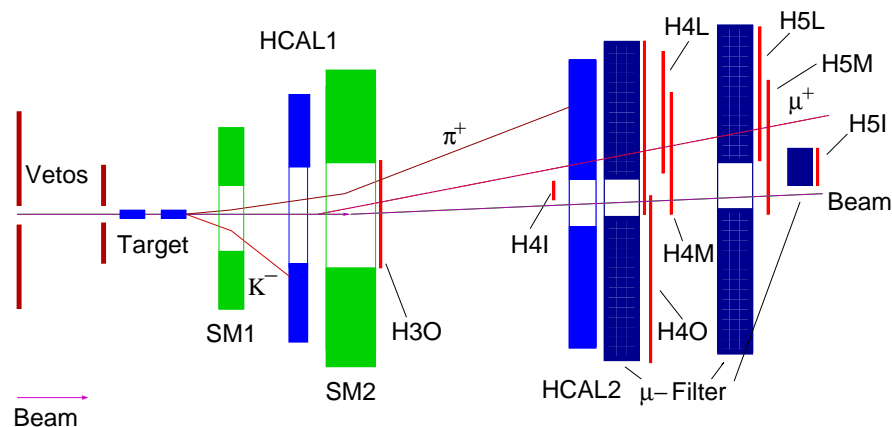


Figure 3.2: Detectors used for the trigger system in COMPASS (not to scale) [28].

3.2.1 The Polarized Target

To reach high statistics despite the small cross-section for muon scattering, COMPASS is operating with a solid state target. Up to 2004, the target system of the SMC³ described in [30] was used. It consists of two target cells, each 60 cm long and a diameter of 3 cm, separated by a gap of 10 cm. The target cells can be polarized in opposite directions. The polarizations are flipped every 8 hours for longitudinal polarization, in order to reduce systematic errors due to acceptance effects. The acceptances for the two cells are different, due to the target magnet. It limits the angular acceptance to about 70 mrad at the upstream end of the target, which gradually increases to 180 mrad at the downstream end. In order to maintain the polarization, the target cells are cooled down to about 50 mK. Until 2006, COMPASS measured on a polarized ⁶LiD target, which can in good approximation be seen as an effective ⁴He + 2D target.

3.2.2 The COMPASS Trigger System

The COMPASS trigger system decides, whether an interesting event has occurred. For $Q^2 \lesssim 20 \text{ GeV}^2$, it is mainly based on the detection of the scattered muon by dedicated trigger hodoscopes, located after thick absorbers. These hodoscopes are combined in the so-called inner, middle, ladder and outer triggers. For the middle and outer trigger, a minimum energy deposit in one of the hadronic calorimeters is required as well. A pure calorimetric trigger (with higher energy threshold) has also been implemented. It extends the kinematic range of the COMPASS experiment to higher Q^2 , where the angle of the scattered muon is so large, that it is not detected with the hodoscopes. The middle trigger hodoscopes are also used as an inclusive trigger, without requiring an hadronic signal. To avoid fake triggers coming from halo muons, a system of veto hodoscopes is installed upstream of the target. A more detailed explanation of the COMPASS trigger system can be found in [31].

³Spin Muon Collaboration

3.2.3 Tracking Detectors

A large variety of tracking devices is used at COMPASS. They can be divided into three groups: Very Small Area Trackers (VSAT), Small Area Trackers (SAT) and Large Area Trackers (LAT). Their resolution in space and time is optimized to the particle flux in different parts of the detector, which varies over more than 5 orders of magnitude. The tracking detectors are usually grouped together into tracking stations. A tracking station typically consists of one VSAT, one SAT and one LAT. The outer region, where the fluxes are rather low, is covered by the LAT, the intermediate region by the SAT and the part closest to the beam by the VSAT.

Table 3.1: Tracking Devices used at COMPASS

VSAT	Scintillating Fibers, Silicon Micro strips
SAT	MICROMesh Gaseous Structure (MICROMEAS), Gas Electron Multiplier (GEM)
LAT	Drift Chambers, Straw Tubes, Multi Wire Proportional Chambers (MWPC)

3.2.4 Particle Identification

Muon Identification

Muons are identified exploiting the fact, that muons are the only charged particles which can pass through a large amount of material. For this reason, there are thick walls of concrete or iron at the end of each stage of the spectrometer, the muon filters. Particles which cause hits in both parts of the muon walls, which are wire chambers located directly in front of and behind the filters, are then identified as muons. Also information from the two hadronic calorimeters can be used to distinguish muons from hadrons, since their energy deposit with respect to their momentum is much lower than the energy deposit of hadrons.

Hadron Identification

Pions and kaons can be identified using the RICH detector, which is located downstream of SM1. The RICH utilizes the fact that a particle with a velocity β higher than the speed of light in the medium with refractive index n emits photons with a characteristic angle Θ_{Ch} to its direction of motion:

$$\cos \Theta_{Ch} = \frac{1}{\beta n} = \frac{1}{n} \sqrt{1 + \frac{m^2}{P^2}} . \quad (3.1)$$

In the second equation Θ_{Ch} is expressed in terms of momentum P and mass m of the particle. Thus it is possible, to determine the particle mass by measuring Θ_{Ch} in addition to the momentum obtained from the tracking. It can be seen from Eq. 3.1, that the minimal velocity for Cherenkov radiation is

$$\beta_{\min} = \frac{1}{n} \quad \Leftrightarrow \quad P_{\min} = \frac{m}{\sqrt{n^2 - 1}} . \quad (3.2)$$

An upper experimental limit $\Theta_{Ch,max}$ exists for $\beta \rightarrow 1$. Different particle types can not be distinguished, as soon as β is close to one for both their masses and both particles emit Cherenkov radiation with an angle of almost $\Theta_{Ch,max}$. Thus it is difficult to separate electrons and pions, since electrons emit Cherenkov radiation with the maximum angle over the whole momentum region covered by the COMPASS Experiment, while pions emit Cherenkov radiation with almost $\Theta_{Ch,max}$ from about 8 GeV. The COMPASS RICH is operated with C_4H_{10} as radiator gas, which has a refractive index of about $n_{C_4H_{10}} - 1 = 0.0015$. In this case, the lower thresholds for Cherenkov radiation are approximately 2.5 GeV for pions, 8.9 GeV for kaons and 17 GeV for protons. The upper limit to separate electrons and pions is about 8 GeV, pions and kaons can be separated up to about 43 GeV.

3.3 Data Reconstruction

The data is digitized directly on the front end cards, temporarily stored on read-out buffers and merged on event builders [32]. Then it is transferred to CASTOR [33], the CERN Advanced STORage manager, where it is again buffered on disks until it is finally written to tape. After the transfer of the acquired data to tape, the raw data is reconstructed using the COmpass Reconstruction and AnaLysis software (CORAL) [34], which is based on C++ and ROOT [35]. At this stage, the physical information, like tracks and momenta of particles or the position of vertices is determined. Both the track and vertex reconstruction are based on a Kalman fit [36], which is a widely used approach in high energy physics for such tasks. More details about the track and vertex reconstruction can be found in [37, 38]. Events containing at least one vertex are stored in mini Data Summary Tapes (mDSTs), which can be processed with another software tool called PHAST (PHysics Analysis Software Tools) [39]. With PHAST, interesting physical events for a particular analysis can be selected and physical quantities calculated. The desired information can then be written into a ROOT tree, so that the final steps of the analysis can be performed easily.

This analysis requires a Monte Carlo (MC) simulation, which simulates both the physical interaction and the detector response. It will be described in Sec. 5.1. Here the events are generated with LEPTO [40]. Afterwards the detector response is simulated with COMGEANT (COMPASS GEometry ANd Tracking). COMGEANT [41] is the detector simulation tool for the COMPASS experiment, based on GEANT 3.21 [42], a program used to simulate the passage of elementary particles through matter. The output of COMGEANT is then similar to the raw data, so it can be reconstructed and analyzed with CORAL and PHAST. Additional information coming from the MC generator is still present in the mDSTs, which allows to estimate detector properties like acceptances or resolutions.

4. Data Selection

Since COMPASS has a broad physics program and thus covers a large kinematic region, not all the recorded events are suitable for a DIS analysis. Therefore a data sample is needed which is enriched with interesting events. Also certain quality criteria have to be fulfilled. The event sample used in this analysis is based on a pre-cut sample for 2004 data, originally produced for the extraction of g_1 [43] for $Q^2 > 1.0 \text{ GeV}^2$. However, only the data taken in the weeks W26 and W27 are used. There are two reasons for this: Firstly, RICH identification is used to reject electrons, an option which was only introduced in a newer version of CORAL. At present, only part of the data¹ has been reconstructed using this newer CORAL version. Secondly there were minor changes to the spectrometer during the weeks W28-W38 [44], which were not taken into account in the presently existing MC simulation. The weeks W22/W23 were not used, since during this time the beam conditions were very different from the nominal ones because of problems in the SPS [45]. Nevertheless, there is still plenty of statistics and the error of the measurement is dominated by the intrinsic uncertainty of the detector simulation. This chapter contains a detailed description of the performed event selection.

4.1 Event Selection

4.1.1 Data Quality

To avoid false modulations due to changes in the spectrometer performance, several criteria (e.g. the number of tracks and the number of vertices per event) are monitored for every spill and are used to reject either complete runs or spills, where the spectrometer performance varies. These spills are grouped together in bad spill lists. These lists as well as further information can be found in [46].

Further, a reasonable quality of the reconstructed tracks is ensured with a cut on

$$\chi_{\text{red}}^2 = \frac{\chi^2}{N_{\text{Hits}} - N_{\text{FitPar}}} < 10 \quad (4.1)$$

for each track. N_{Hits} is the number of hits associated with the track, $N_{\text{FitPar}} = 5$ the number of fitted parameters. The five parameters determined for each track are the positions X , Y , the derivatives dX/dZ , dY/dZ , and the ratio $q/|P|$ of charge q and

¹the data taken in the periods W22, W23, W26, W27, W38, W39, W40

momentum P , all at a fixed Z position² [37]. Also a cut on $\chi_{\text{red, vertex}}^2 < 2$, which for a vertex with N_{track} tracks is given by

$$\chi_{\text{red, vertex}}^2 = \frac{\chi_{\text{vertex}}^2}{2N_{\text{track}} - 3}, \quad (4.2)$$

[38] is applied for the primary vertex. Additionally, tracks which leave the detector before the first spectrometer magnet are excluded from this analysis by demanding the last hit Z_{last} to be behind SM1 ($Z_{\text{last}} > 3.50$ m).

4.1.2 Kinematic Range

In order to select DIS events, $Q^2 > 1$ GeV² is required. A cut on the invariant mass $W > 5$ GeV avoids the resonance region of the cross section. Additionally the relative energy loss of the lepton y is restricted to $0.1 < y < 0.85$. The lower cut is to ensure good resolution in y and to eliminate elastic scattering events, while the upper cut discards events where radiative corrections become important.

Furthermore, the sum of the relative energies z_h^i of the hadrons i in the event has to fulfill

$$\sum_{\text{hadrons } i} z_h^i < 0.85 \quad (4.3)$$

to exclude decay products of exclusively produced mesons (see Fig. 4.1), since these processes are not included in the MC simulation.

4.1.3 The Primary Vertex

If a beam particle is found and assigned to a vertex, the vertex is called a primary vertex. It is required to be inside the target. For this reason, the distance of the vertex to the target axis must be smaller than 1.4 cm. Also the target material has a tendency to settle down, so there is less material in the upper part of the target cell than in the lower one. Therefore, a cut on the Y coordinate of the primary vertex of $Y < 1.0$ cm is applied. In some events, more than one primary vertex is reconstructed. In this case, only the so called "best" primary vertex is taken, which is the one with the most outgoing tracks or in case of equal number of tracks the one with the best χ_{red}^2 . In addition to the detection of the incoming and outgoing muon, at least one additional outgoing track, considered as a hadron candidate, is required. All these particles have to pass additional cuts described below to be considered in the analysis.

4.1.4 Beam and Scattered Muon

Both the incoming and the outgoing muon have to be reconstructed to be able to calculate the DIS variables. If more than one positively charged outgoing muon is

²the coordinate system in the Lab system is oriented as follows: the nominal beam direction defines the Z axis, the Y axis is oriented upwards and to make the coordinate system right handed, the X axis points towards the left side, when looking along the direction of the beam. The origin is at the nominal target position, as shown in Fig. 3.1

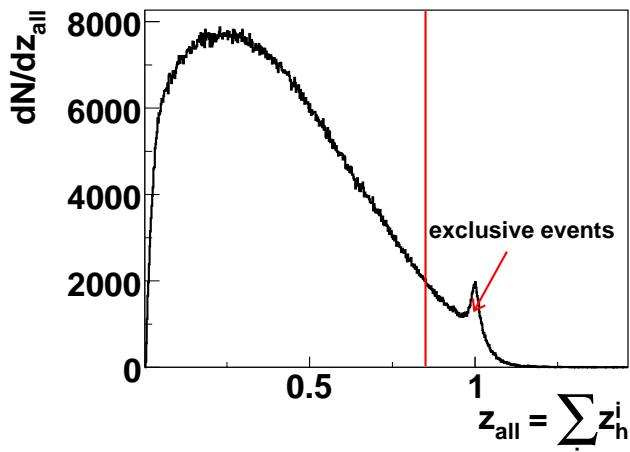


Figure 4.1: z_{all} distribution. The peak comes from the decay products of exclusively produced mesons (mainly pions from ρ decays). The red line indicates the cut on z_{all} .

found, the event is discarded. In addition, information of the two Muonwalls (MW) located after thick absorbers (see sec. 3.2.4) is used to search for muons not identified as such with the reconstruction software. If the track of the hadron candidate has at least four hits in MW1 or at least six hits in MW2, it is considered to be a muon and the event is discarded as well. To ensure the reliability of the muon identification the muon track has to have traversed an amount of detector material corresponding to at least 30 radiation lengths X_0 . The momentum of the beam muon has to be between 120 and 200 GeV and the extrapolated beam track has to cross both target cells to equalize the fluxes in the upstream and downstream cell.

In some events, the scattered muon goes through the hole of the first absorber and does not cross the second absorber and thus has not penetrated enough material to be identified as a muon. If an additional positive muon is created in the interaction, this is falsely identified as the scattered muon. This leads to an incorrect calculation of all kinematical variables and thus these events have to be rejected. A set of cuts based on geometrical considerations has been introduced in [47] to remove these events. The tracks of all hadron candidates are extrapolated to the downstream end of the spectrometer at $Z = 50$ m. Then the extrapolated positions X_e and Y_e in the plane orthogonal to the beam axis must lie outside the following regions:

$$\sqrt{(X_e - 45 \text{ cm})^2 + Y_e^2} < 10 \text{ cm} \quad (4.4)$$

if the last hit of the track Z_{last} was before SM2 ($Z_{\text{last}} < 20$ m) or

$$\begin{aligned} \sqrt{(X_e - 35 \text{ cm})^2 + Y_e^2} < 15 \text{ cm} \quad \text{or} \\ |X_e - 55 \text{ cm}| < 13 \text{ cm} \quad \text{and} \quad |Y_e| < 3 \text{ cm} \end{aligned} \quad (4.5)$$

if the last hit was after SM2. Events where a hadron candidate had a hit after the last muon absorber ($Z = 38$ m) were rejected as well.

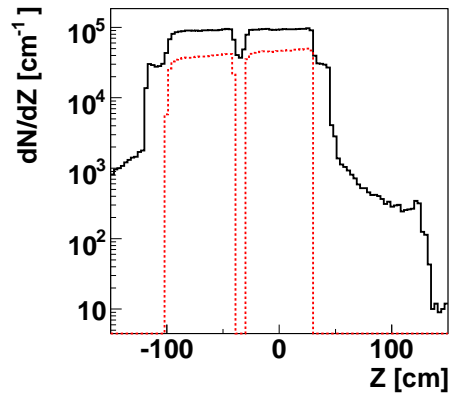


Figure 4.2: Z position of the primary vertex without cuts (black curve) and after all cuts, in particular the requirement to be inside the target (red dotted curve).

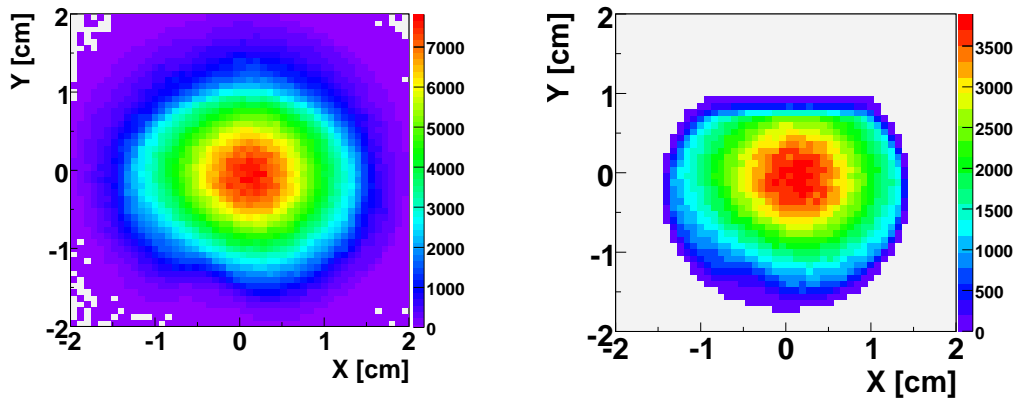


Figure 4.3: distribution of primary vertices in the $X - Y$ plane before cuts (left) and after cuts(right).

After all cuts, about 4 million DIS events with at least one hadron surviving the cuts described below remain. An overview over the effect of each cut is given in Tbl. 4.1 at the end of this chapter.

4.2 Hadron Selection

Apart from the scattered muon, one or more additional outgoing particles have to be detected. These hadron candidates have to fulfill additional requirements in order to suppress contamination by muons and electrons. To reduce the number of muons treated as hadrons, a minimum energy deposit in one of the hadronic calorimeters is required. As depicted in Fig. 4.4, the threshold is 4 GeV for HCAL1 and 5 GeV for HCAL2. Furthermore, the hadron is discarded if it has clusters in both hadronic calorimeters. For the same reason, a cut on the amount of traversed material (in radiation lengths) $X/X_0 < 10$ is applied.

To reject electrons, RICH identification is used, which will be described in section 4.4. Electrons could in principle also be identified using the electromagnetic calorimeter in the SAS, but ECAL2 was not fully operational during the 2004 run. For this reason ECAL2 was not used in the analysis.

Furthermore a minimum polar angle of the hadron in the lab system of $\theta_{h,\text{LAB}} > 20$ mrad is applied. The reason for this cut is to remove a peak in the ϕ_h distribution at $\phi_h \approx 0$ (see Fig. 4.6), which is thought to come from photons converting to electron-positron pairs. To ensure that the track really comes from the primary vertex, the first hit Z_{first} of the hadron track has to be in front of the first spectrometer magnet ($Z_{\text{first}} < 3.50$ m). As can be seen in Fig. 4.5, there are several tracks where this is not the case. There are two main reasons for this: The first is the way tracking is performed in the COMPASS experiment [37]. In a first stage, partial tracks are fitted in regions with only weak magnetic fields, where the tracks are essentially straight lines. In a second step, the track is bridged between these segments using a track dictionary, and the final track parameters are obtained by fitting the complete track. So if the first track segment is missing, because there are not enough hits, or searched at the wrong position because of problems in the bridging procedure, the track will only start after SM1. The other main reason is of course, that the track could also physically start after SM1, if the particle is created from a neutral particle, e.g. photon conversion to an electron-positron pair. Finally, a minimum transverse momentum (w.r.t. the photon direction, cf. Fig. 2.3) $P_t^h > 0.1$ GeV is required, to ensure ϕ_h is well defined. In total, a bit more than 6.5 million hadrons pass the cuts above, again an overview over the effect of each cut is presented in Tbl. 4.2 at the end of this chapter.

4.3 Leading Hadron Selection

The Cahn effect is a prediction made for struck quarks. These quarks are mostly contained in the hadron with largest energy fraction z_h . Therefore a subsample enriched with these quarks is created containing only the hadrons with largest z_h . To ensure

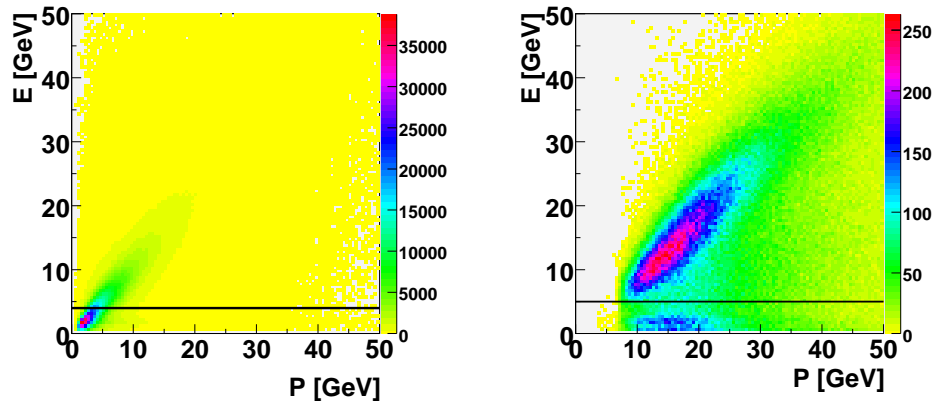


Figure 4.4: Correlation between measured energy in the calorimeter and the reconstructed momentum for HCAL1 (left) and HCAL2 (right). The red lines indicate the minimum required energy deposit for the particle to be accepted as a hadron. Note that most of the hadrons end up in HCAL1.

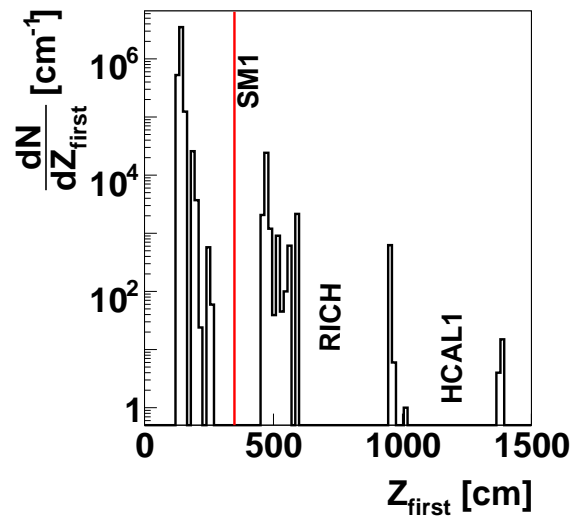


Figure 4.5: The position of the first hit of each track. If the first hit is after SM1, the particle is rejected.

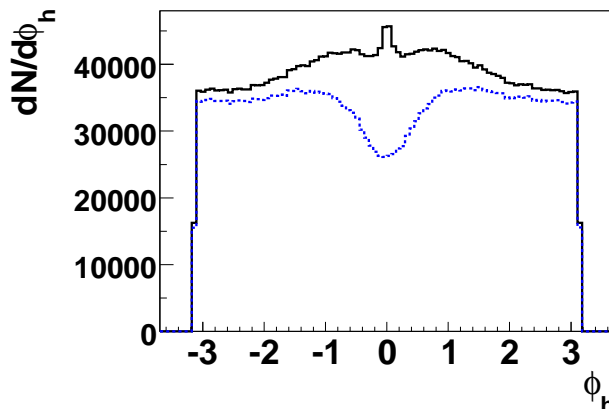


Figure 4.6: ϕ_h distribution without (black line) and with (blue dotted line) a cut on $\theta_{h,\text{LAB}}$. The correlation between $\theta_{h,\text{LAB}}$ and ϕ_h will be discussed in Sec. 5.4.

that the detected leading hadron really is the leading one, it has to fulfill additional requirements: If the missing energy

$$z_{\text{miss}} = 1 - z_{\text{all}} = 1 - \sum_{\text{hadrons}} z_h^i \quad (4.6)$$

in the event is bigger than z_h of the leading hadron, it is possible, that the real leading hadron was a neutral particle which did not leave a track in the spectrometer. The signature of a neutral particle would be a cluster in one of the calorimeters with no track assigned. Thus the two hadronic calorimeters are searched for such clusters with energy E_{Cluster} with $E_{\text{Cluster}} + 2\Delta E_{\text{Cluster}} > E_h$ and no assigned track. In this equation E_h is the energy of the leading hadron, obtained from momentum and assigned mass. The resolution $\Delta E_{\text{Cluster}}$ for the two hadronic calorimeters is given by [28]:

$$\frac{\Delta E_{\text{HCAL1}}}{E_{\text{HCAL1}} [\text{GeV}]} = \sqrt{\frac{0.59^2}{E_{\text{HCAL1}} [\text{GeV}]} + 0.076^2} \quad (4.7)$$

$$\frac{\Delta E_{\text{HCAL2}}}{E_{\text{HCAL2}} [\text{GeV}]} = \sqrt{\frac{0.66^2}{E_{\text{HCAL2}} [\text{GeV}]} + 0.05^2} \quad (4.8)$$

If no such cluster is found, the leading hadron is accepted, else rejected. Additionally, the energy fraction z_{lead} of the leading hadron has to be bigger than $z_{\text{lead}} > 0.25$. As can be seen in Fig. 4.7, for $z_{\text{lead}} < 0.25$ the leading hadron is often not correctly identified. After all these cuts, about 1.3 million leading hadrons remain to be used in this analysis.

4.4 Particle Identification

Although the analysis was done for a sample containing all kinds of (charged) hadrons, i.e. mainly pions and some kaons and protons, RICH information was used to identify

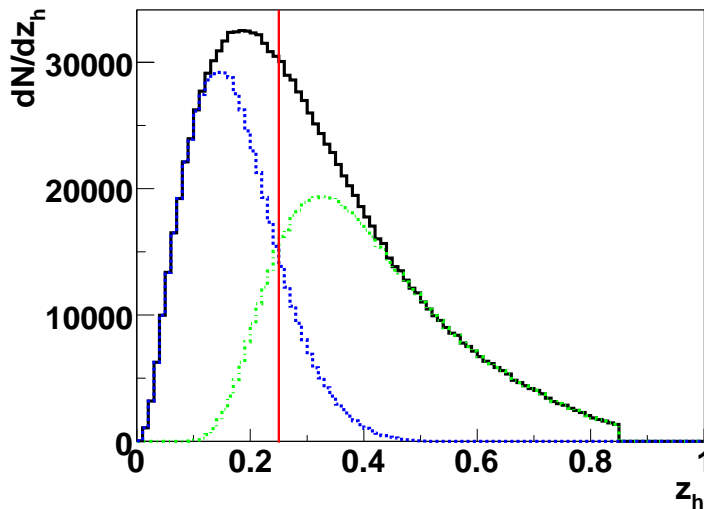


Figure 4.7: MC: Distributions of identified leading hadrons (black curve), correctly identified leading hadrons (dashed-dotted green curve) and incorrectly identified leading hadrons (blue dotted curve). The vertical red curve indicates the cut $z_h > 0.25$ for the leading hadron sample.

the hadron type, whenever possible. The ϕ_h distribution itself relies only on the measured momentum and thus is independent of the assigned mass. However, for correct calculation of the hadronic energy fraction z_h , the particle mass has a small impact. As described in Sec. 3.2.4, the RICH allows to reconstruct the velocity β from the measured angle Θ_{Ch} of the Cherenkov radiation. Since the momentum can be obtained from the tracking, it is possible to determine the particle mass. To allow identification, the particle has to have a momentum inside the range, where the RICH allows identification and the RICH has to have found a Cherenkov ring belonging to the track, see Fig. 4.8.

Since the refractive index of the RICH radiator gas changes slowly in time due to atmospheric pressure and temperature variations, the minimum thresholds P_{\min} for Cherenkov radiation are calculated for every event. In order to ensure a reasonable number of Cherenkov photons, the actual minimal required momenta have to be at least $P_{\min} + 0.5$ GeV for pions and $P_{\min} + 1.0$ GeV for kaons and protons. Electrons always emit Cherenkov radiation in the momentum range covered by the COMPASS spectrometer. During the reconstruction with CORAL, for each track with RICH information, a likelihood L is calculated for mass hypotheses of pions, kaons, protons, electrons and muons. Also a likelihood L_{BG} for the case where the ring is coming from background in the RICH (electronic noise, other particles in the event, etc.) is calculated. The muon likelihood cannot be used, since the RICH is incapable of distinguishing between pions and muons, due to their similar masses. More information about hadron identification with the RICH can be found in [48, 49]. In this analysis,

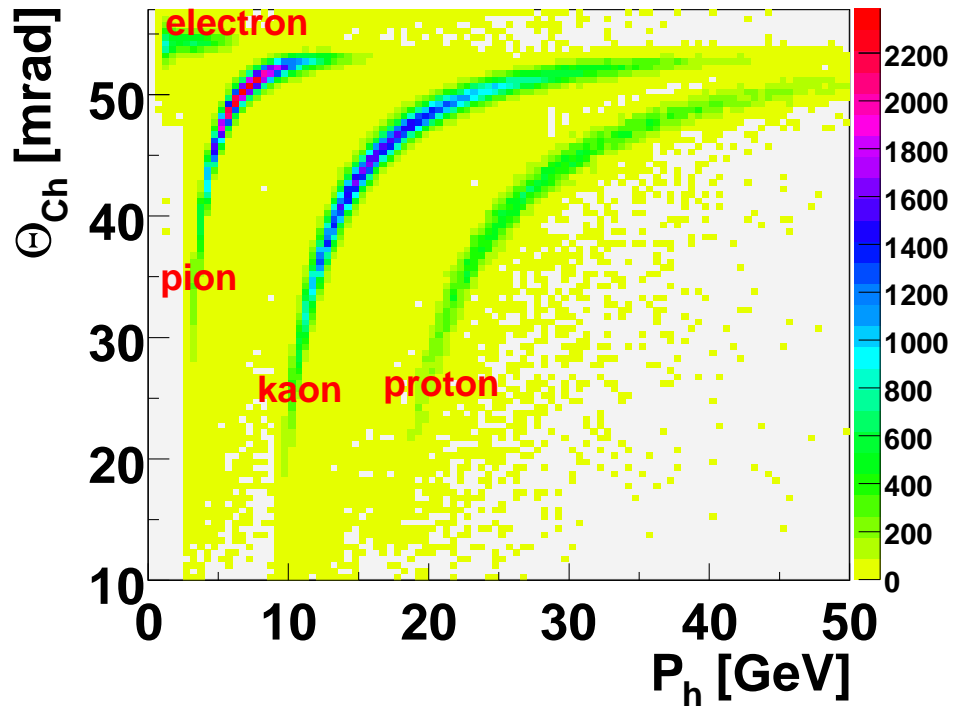


Figure 4.8: The correlation of the reconstructed Cherenkov angle with the measured momentum for pions, kaons, protons and electrons. The pion band is suppressed by a factor of 10 and the proton band is enhanced by a factor of 6, also the criteria for the identification are different than the ones used for the analysis.

the particle is assumed to be of the most likely type, if the maximum likelihood L_{\max} fulfills

$$L_{\max} > C_{2\text{ndmax}} L_{2\text{ndmax}} \quad \text{and} \quad L_{\max} > C_{\text{BG}} L_{\text{BG}}, \quad (4.9)$$

where $L_{2\text{ndmax}}$ is the second largest likelihood. The factors $C_{2\text{ndmax}}$ and C_{BG} depend on the particle type and are listed in Tbl. A.1 in App. A.2. If no identification with the RICH is possible, the hadron is assumed to be a pion. If the hadron candidate is identified as an electron, it is discarded.

Table 4.1: Event Statistics

Cut	rejected vertices	remaining vertices [%]	vertices after cut
total number of primary vertices			11240118
at least two outgoing particles	2173914	81	9066204
scattered muon found* and unique	398563	96	8667641
best primary vertex	79512	99	8588129
Inside target	2144077	75	6444052
beam momentum	780	100	6443272
x/x_0	293949	95	6149323
$\chi_{\text{red}}^2 < 10$ for muon tracks	22786	100	6126537
$0.1^* < y < 0.85$	93950	98	6032587
$Q^2 > 1.0 \text{ GeV}^2^*$, $W > 5 \text{ GeV}^*$	13	100	6032587
equal flux	308827	95	5723747
vertex $\chi_{\text{red}}^2 < 2$	317216	95	5406531
z_{all}	305923	95	5100608
extrapolation and Z_{last} Cuts	38847	99	5061761
≥ 1 hadron passing all cuts (cf. Tbl. 4.2)			4218388

*was already applied in the precut sample

Table 4.2: Hadron Statistics

Cut	rejected hadrons	remaining hadrons[%]	hadrons after cut
hadron candidates			13049559
Z_{first} before SM1	77265	99	12972294
Z_{last} after SM1	426810	97	12545484
$\chi_{\text{red}}^2 < 10$	419920	97	12125564
x/x_0	82568	99	12042996
HCAL cuts	2406216	80	9636780
RICH ID electron	869794	91	8766986
P_t^h	1084006	88	7682980
$\theta_{h,\text{LAB}}$	988231	87	6694749
final hadrons			6694749
final leading hadrons			1322592

5. Acceptance Correction and Determination of the ϕ_h Dependence

This chapter describes how the modulations of the cross section are determined from the measured count rates. In order to avoid false modulations due to the detector acceptance, a MC simulation is used to correct detector acceptance effects. Therefore a brief introduction to Monte Carlo simulation in general and the tools used for the MC simulation in the COMPASS experiment is given in Sec. 5.1 as well as a short comparison between data and MC. Since the moments of the cross section are determined using a fit to binned histograms, the choice of binning is explained in Sec. 5.2. The acceptance correction applied to the measured count rate to compensate the non-uniform acceptance of the apparatus will be described in Sec. 5.3, leading to a discussion of the acceptance in Sec. 5.4. Finally, all the steps necessary to extract the moments of the cross section are summarized in Sec. 5.5.

5.1 Data and MC

Although the term Monte Carlo (MC) in principle only describes the use of random numbers to solve an integral numerically, the term MC simulation in the context of particle physics usually implies the use of these techniques to simulate physical processes and the detector response to these. The use of MC simulations is the only viable way to estimate the performance of the complex detector systems used in particle physics. In order to compare measured distributions with simulated ones, the simulation has to include several steps. This often referred to as a MC chain and is depicted schematically in Fig. 5.1: First, the physical reaction is simulated using a MC generator, e.g. LEPTO [40] or PYTHIA [50]. In a second step, the detector response of a particular experiment is simulated. The output of these detector simulation tools has to be in a similar format than the measured data, so that in the last step the MC data can be reconstructed analogously to data. For this thesis, the scattering process is simulated with LEPTO using only leading order matrix elements and the detector response with COMGEANT [41], the detector simulation tool for the COMPASS experiment. Afterwards the simulated data is reconstructed with CORAL and then the same event selection as for real data can be performed for the reconstructed MC data using PHAST. In the following, the term generated MC (data) will be used for the output of the MC generator alone, while the term reconstructed MC is used for the output of the full MC chain, including detector simulation and reconstruction.

To ensure that the MC simulation describes the apparatus properly, a good agreement between real data and reconstructed MC is mandatory. Fig. 5.2 shows the x, Q^2, y, z_h

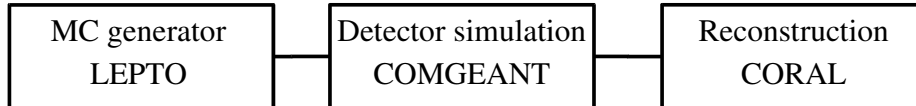


Figure 5.1: The MC chain for the COMPASS experiment.

and P_t^h distributions for both real and MC data. The agreement is mostly satisfactory, apart from a strong disagreement for $P_t^h \gtrsim 1$ GeV. This disagreement for large P_t^h is expected, since the QCD contributions described in Sec. 2.5.3 are important there, but are not included in the MC simulation. This illustrates that, since it is not possible to include all possible processes in the MC simulation, differences between real and MC data are possible. Disentangling these effects from effects due to non-optimal detector description can be very difficult.

5.2 Resolution and Binning

In general, a resolution for an observable x can be estimated from MC by calculating the difference between the generated x_{gen} and the reconstructed quantity x_{rec} :

$$\Delta x = x_{\text{gen}} - x_{\text{rec}} . \quad (5.1)$$

Since the modulations in the azimuthal angle ϕ_h are determined using fits to binned histograms, the resolution in ϕ_h is important: The number of bins has to be a compromise between the need to have enough bins to fit a function with four parameters (Eq. 5.7 to the histogram and the requirement, that the bin width is considerably larger than the angular resolution of the measurement to avoid smearing effects. A limit for the number of bins is also given by the available data: the statistics in each bin has to remain large enough for a meaningful measurement. In order to obtain the dependencies for various kinematical variables, the sample is further divided into several kinematic bins.

The obtained resolution for ϕ_h is shown in Fig. 5.3, leading to a choice of 18 bins in ϕ_h . For the kinematic binning, the situation is slightly more complex, since the resolution depends on the value of the variable. Also the bins are not equidistant but chosen in such a way that each bin contains a similar number of events. However, each kinematic bin is large enough that smearing effects are negligible. For each kinematical bin, the azimuthal angle ϕ_h is calculated according to Eq. 2.11 and 2.12 and filled into a histogram of 18 equidistant bins ranging from $-\pi$ to π .

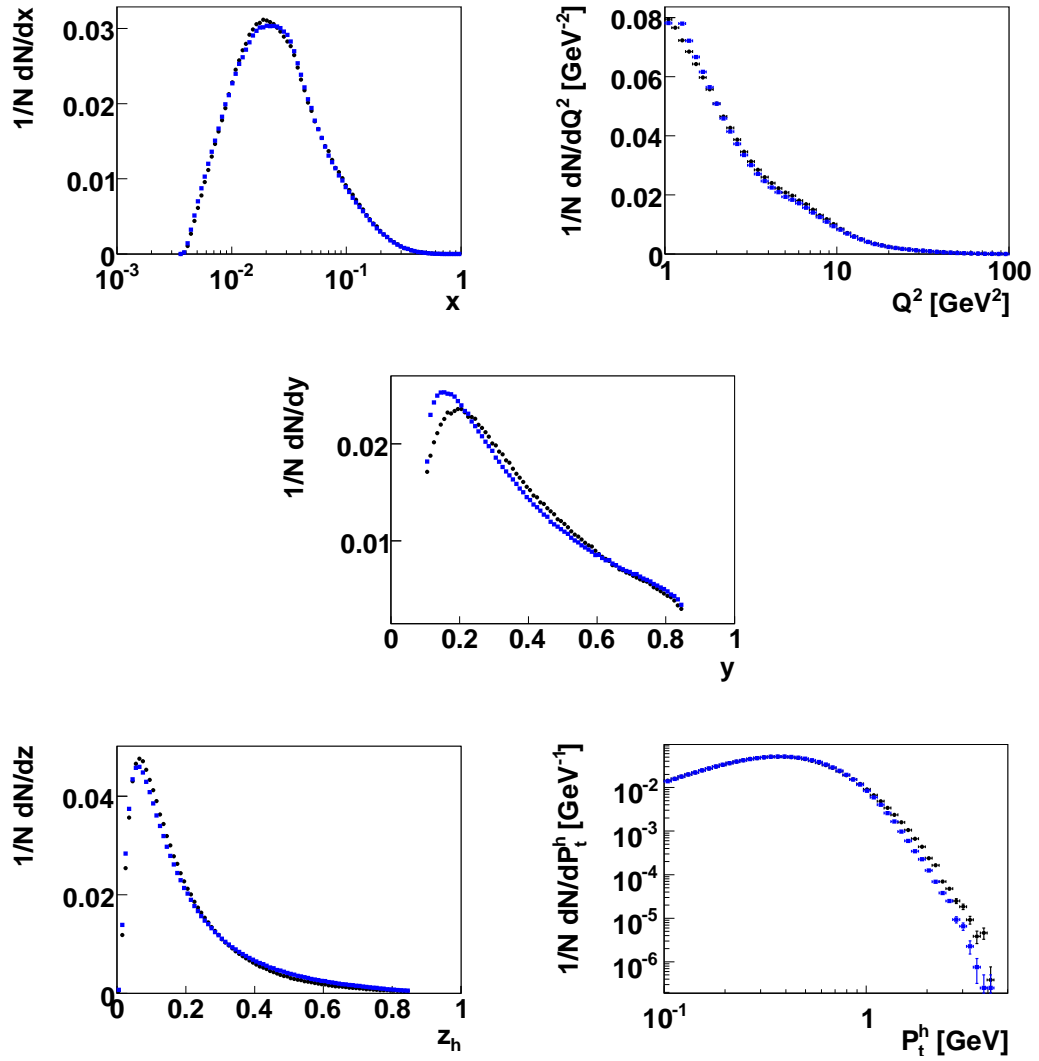


Figure 5.2: x , Q^2 , y , z_h and P_t^h distributions for data (black circles) and MC (blue squares).

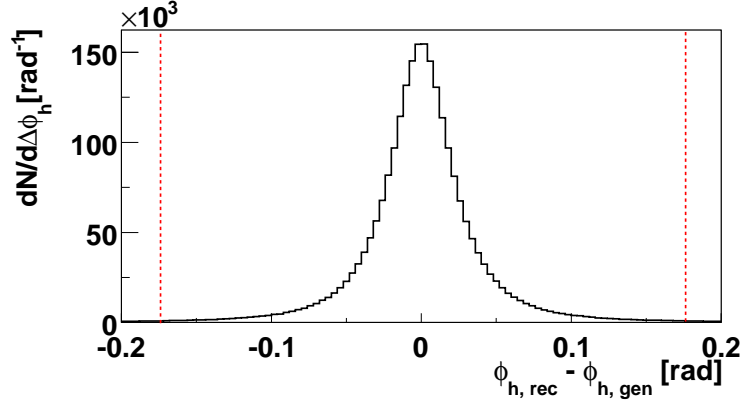


Figure 5.3: Difference between reconstructed and generated ϕ_h . The two dotted red lines indicate the chosen bin width.

5.3 The Acceptance Correction

The acceptance A of the COMPASS Spectrometer as a function of ϕ_h is obtained for each kinematic bin from the generated and reconstructed angular distributions via

$$A(\phi_h) = \frac{N_{\text{rec}}(\phi_h)}{N_{\text{gen}}(\phi_h)}, \quad (5.2)$$

where $N_{\text{gen (rec)}}(\phi_h)$ is the number of generated (reconstructed) hadrons in a given ϕ_h bin. While for the reconstructed hadrons the same cuts are applied than for real data, the only requirement on the generated data is that the events lie in a similar kinematic region ($Q^2 > 1 \text{ GeV}^2$, $0.09 < y < 0.9$ and for the acceptance corrections for leading hadrons $z_h > 0.25$) than the real data. No leading hadron selection is performed on the generated distributions, since the number of reconstructed hadrons has to be a subsample of the number of generated ones. Since the leading hadron selection described in Sec. 4.3 does not always identify the correct leading hadron, this would not be the case anymore, if for the generated ϕ_h distribution only real leading hadrons are considered.

$A(\phi_h)$ can be interpreted as the probability for a hadron emitted under the angle ϕ_h to be detected in the spectrometer and to survive the cuts described in the previous chapter. So strictly speaking this quantity should be called a pseudo acceptance, since it depends on the cuts applied in the event selection. $N_{\text{rec}}(\phi_h)$ follows a binomial

distribution, since the particle is either reconstructed or not, and thus the error of the acceptance function is

$$\sigma_A(\phi_h) = \sqrt{\frac{A(\phi_h)(1 - A(\phi_h))}{N_{\text{gen}}(\phi_h)}}. \quad (5.3)$$

The corrected counting rates $N_{\text{corr}}(\phi_h)$ are then obtained from the measured rates $N_{\text{meas}}(\phi_h)$ as

$$N_{\text{corr}}(\phi_h) = \frac{N_{\text{meas}}(\phi_h)}{A(\phi_h)} \quad (5.4)$$

with the error (the ϕ_h dependencies are suppressed here for simplicity)

$$\sigma_{N_{\text{corr}}}(\phi_h) = N_{\text{corr}} \sqrt{\left(\frac{\sigma_{N_{\text{meas}}}}{N_{\text{meas}}}\right)^2 + \left(\frac{\sigma_A}{A}\right)^2} = N_{\text{corr}} \sqrt{\frac{1}{N_{\text{meas}}} + \left(\frac{1 - A}{AN_{\text{gen}}}\right)^2}, \quad (5.5)$$

which follows with Gaussian error propagation. The MC simulation contains more statistics than the data sample, so this error is dominated by N_{meas} .

In order to improve the acceptance correction, an additional correction for the efficiencies for middle and outer trigger hodoscopes was performed, since both triggers were found to have inefficient slabs. To this end, the scattered muon track in the real and the reconstructed MC data was extrapolated to $Z = 40$ m. Then the extrapolated radial positions X_{Ext} and Y_{Ext} distributions are compared to the distributions obtained from data. In case of strong disagreement, efficiencies are introduced in the MC data to compensate. This is exemplarily shown in Fig. 5.4 for the middle trigger in the period W27. Since it is much faster to introduce the efficiencies offline, they were not included directly in the MC simulation. Also these inefficiencies are time dependent, so MC with different settings for the two different periods would have been necessary. Since the effects on both kinematical and ϕ_h distributions were found to be small, and MC production is time consuming, this was not necessary. The obtained acceptances for upstream and downstream cell are exemplarily shown in Fig. 5.5 for a small, medium and large x bin and will be discussed in the next section.

5.4 The Acceptance of the COMPASS Spectrometer

As can be seen in Fig. 5.5, the acceptance depends strongly on the kinematic bin and also on the target cell: The acceptance of the downstream cell is higher than for the upstream one. While in the low x region, the acceptance decreases towards small $|\phi_h|$, for larger x the situation is inverse and the acceptance drops strongly with larger $|\phi_h|$. In order to understand this behavior, studies on generated MC data were performed. It turned out, that these effects are due to the differences in angular acceptance: The acceptance in the polar angle of the hadron in the lab system $\theta_{h,\text{LAB}}$ increases from 70 mrad for the upstream end of the target to 180 mrad at the downstream end because of the limited acceptance of the target magnet. As can be seen in Fig. 5.6 (top row), an upper bound on $\theta_{h,\text{LAB}}$ causes mainly a loss of events at large $|\phi_h|$, while a lower cut causes a loss at small $|\phi_h|$ (bottom row). This can be understood with Fig. 5.8:

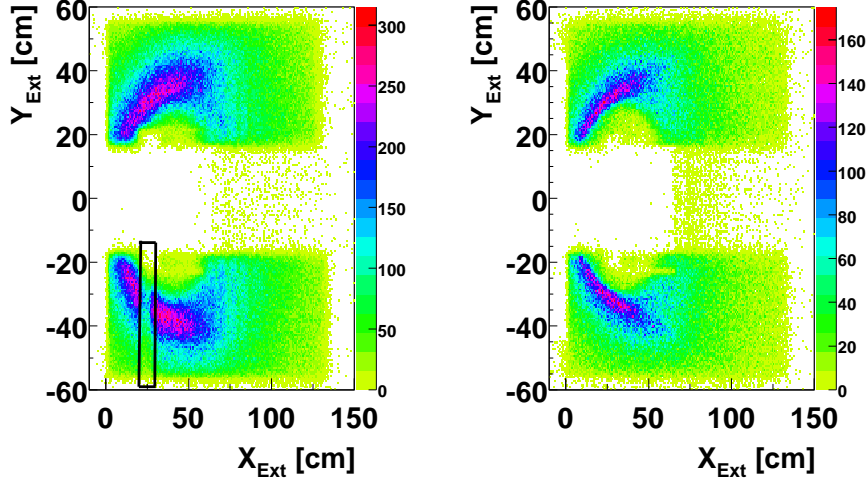


Figure 5.4: distributions of the positions X_{Ext} and Y_{Ext} of the extrapolated muon track for data(left) and MC before the correction(right). The black box at $20 \text{ cm} < X < 30 \text{ cm}$, $Y < 0 \text{ cm}$ indicates an inefficient slab.

ϕ_h is the azimuthal angle of the hadron, in the coordinate system, where the photon direction¹ defines the Z axis. Considering only the case, where the hadron is emitted in the lepton scattering plane, there are two cases: $\phi_h = 0$ corresponds to the hadron going towards the scattered muon, while $\phi_h = \pi$ means that the scattered hadron moves away from the scattered muon. As can be seen in Fig. 5.8, $\theta_{h,LAB}$ tends to be larger for $\phi_h = \pi$ than for $\phi_h = 0$. Thus the acceptance for events with larger $|\phi_h|$ is lower in the upstream cell, where the maximal accepted angle is smaller than for the downstream cell. Since a large polar angle typically means large x , this is especially important in the large x bins. Due to the different angular acceptances this loss starts at lower x for the upstream cell than for the downstream one. This can be seen in the middle plots of Fig. 5.5, where the acceptance at large $|\phi_h|$ decreases more for the upstream cell than for the downstream cell. This cell dependence is the main reason, that the analysis, in particular the acceptance correction, is performed for upstream and downstream cell separately.

5.5 Determination of the Moments of the Cross Section

For reasons given in the previous paragraph, the whole analysis is done for the upstream and downstream cell separately. In order to extract the dependence of the amplitudes of the modulations for the kinematical variables x, y, Q^2, z_h, P_t^h , the data is divided into about 10 kinematic bins for one of the kinematic variables², while the dependence on the other variables are integrated out. Then, since COMPASS measures with a polarized

¹the definition of ϕ_h is depicted again in Fig. 5.7 for convenience.

²The binning can be found in Tbl. A.2 in the Appendix

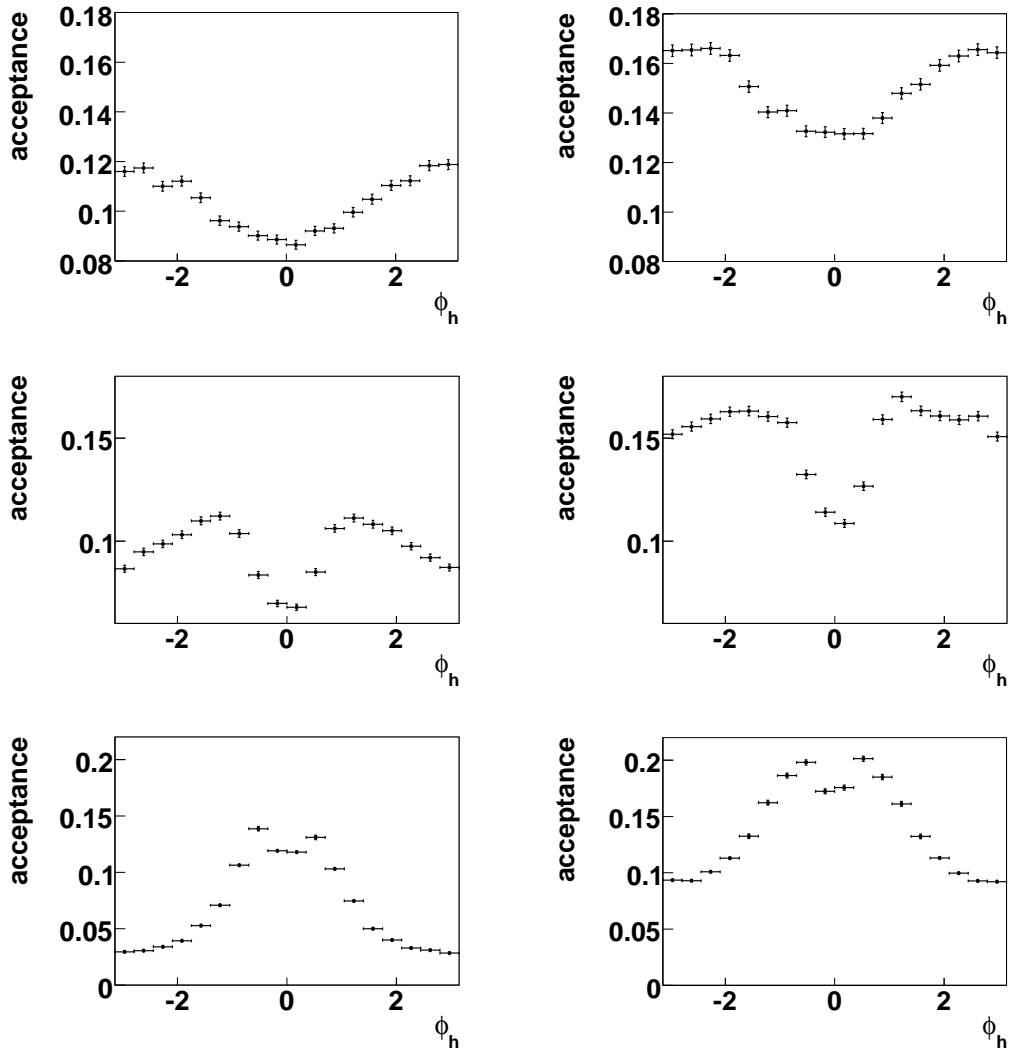


Figure 5.5: Acceptances of the COMPASS spectrometer for positive hadrons in the first (top row, $x < 0.008$), fourth (middle row, $0.02 < x < 0.026$) and eighth (bottom row, $0.08 < x < 1$) x bin each for upstream (left) and downstream cell (right).

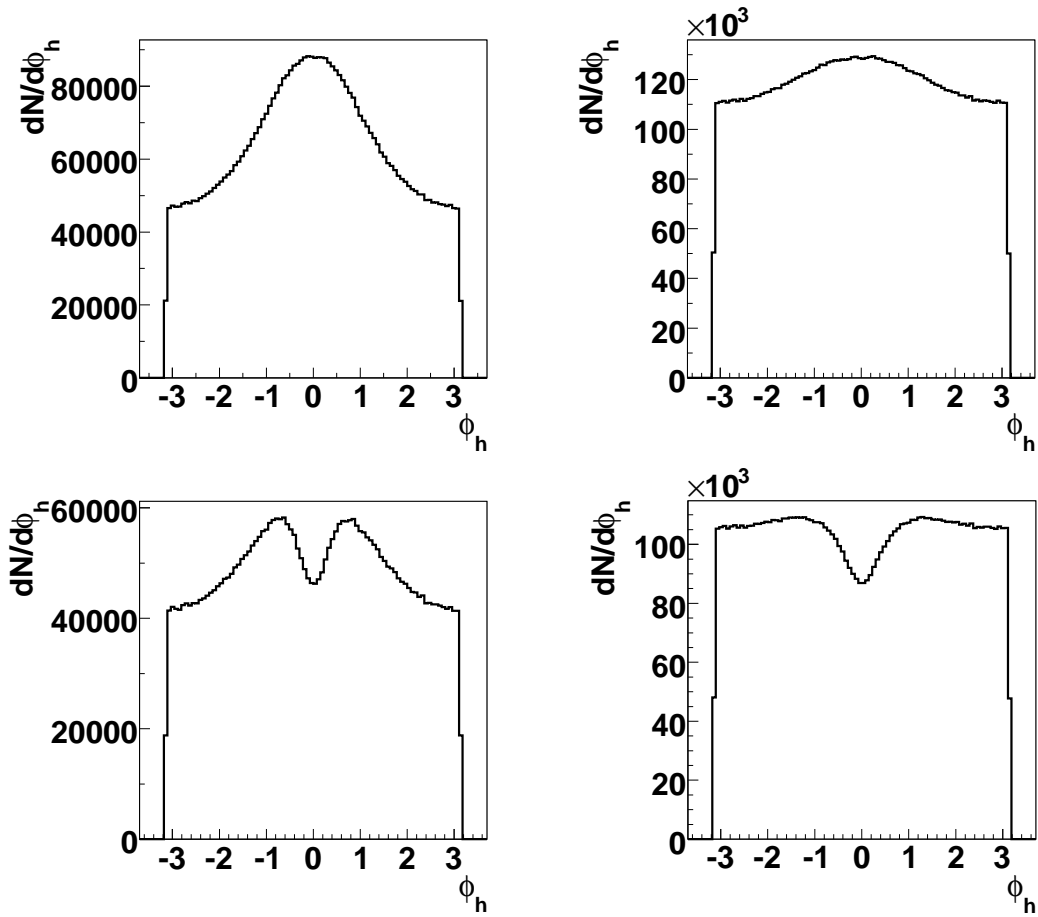


Figure 5.6: generated ϕ_h distribution with different cuts on $\theta_{h,\text{LAB}}$: <70 mrad (top left, acceptance at the upstream end), $\theta_{h,\text{LAB}} < 180$ mrad (top right, acceptance at the downstream end), $20 \text{ mrad} < \theta_{h,\text{LAB}} < 70$ mrad (bottom left) and $20 \text{ mrad} < \theta_{h,\text{LAB}} < 180$ mrad (bottom right).

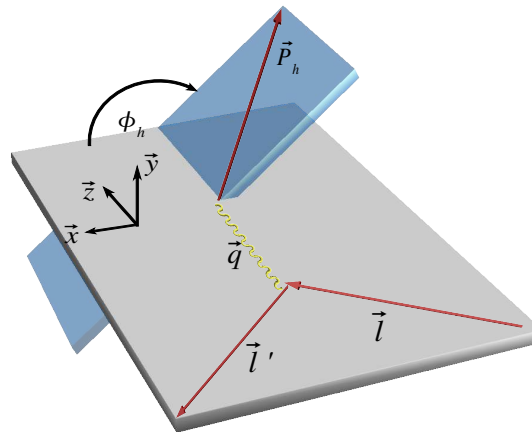


Figure 5.7: Definition of the hadron azimuthal angle ϕ_h as already depicted in Fig. 2.3.

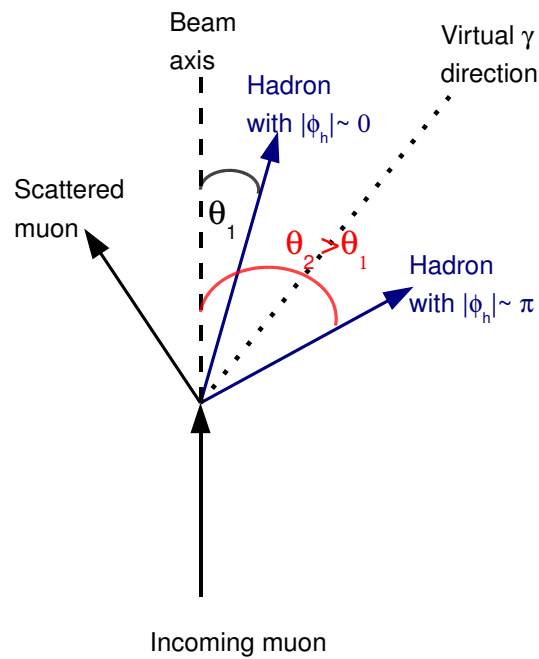


Figure 5.8: A schematic picture of the scattering process in the lab frame for the case, when the hadron is produced in the lepton scattering plane. If the hadron goes in the same direction as the scattered muon, with respect to the virtual photon, $\phi_h = 0$ and the polar angle in the lab frame is smaller than for the case, where the hadron goes in the opposite direction.

target, the data taken with different target polarizations $N_{\leftarrow}, N_{\rightarrow}$ are combined in the following way to ensure that the mean polarization vanishes:

$$N = N_{\rightarrow} + \frac{P_{\rightarrow}}{P_{\leftarrow}} N_{\leftarrow} . \quad (5.6)$$

with $P_{\rightarrow} = \sum_i P_i^{\rightarrow}$ and $P_{\leftarrow} = \sum_i P_i^{\leftarrow}$, where $P_i^{\rightarrow(\leftarrow)}$ denotes the absolute value of the target polarization for event i and the sum runs over all events taken in one configuration, i.e. the target cell either polarized along the beam (P_i^{\rightarrow}) or in the opposite beam direction (P_i^{\leftarrow}).

Afterwards the count rates are corrected for acceptance effects as described above and then fitted with

$$A_0 + A_{\sin \phi_h}^{\text{raw}} \sin \phi_h + A_{\cos \phi_h}^{\text{raw}} \cos \phi_h + A_{\cos 2\phi_h}^{\text{raw}} \cos(2\phi_h) . \quad (5.7)$$

This is exemplarily shown for all hadrons, where the primary vertex was in the upstream cell in Fig. 5.9. From these amplitudes, the moments can be extracted according to Eq. 2.15 and divided by the mean values of the y -dependent functions defined in Eqs. 2.20 and 2.21. These values are about 0.9 for $D_{\cos \phi_h}$ and 0.45 for $D_{\cos 2\phi_h}$, but vary about 10% dependent on the bin. To distinguish between the y -dependent moments $\langle \cos n\phi_h \rangle$ and the corrected ones $A_{\cos n\phi_h}$, the following notation will be used in the next chapter, which contains the discussion of the results:

$$A_{\cos n\phi_h} = \frac{\langle \cos n\phi_h \rangle}{\langle D_{\cos n\phi_h}(y) \rangle} = \frac{A_{\cos n\phi_h}^{\text{raw}}}{2A_0 \langle D_{\cos n\phi_h}(y) \rangle} . \quad (5.8)$$

Finally, the results for upstream and downstream cell and the two periods can be combined taking the weighted mean.

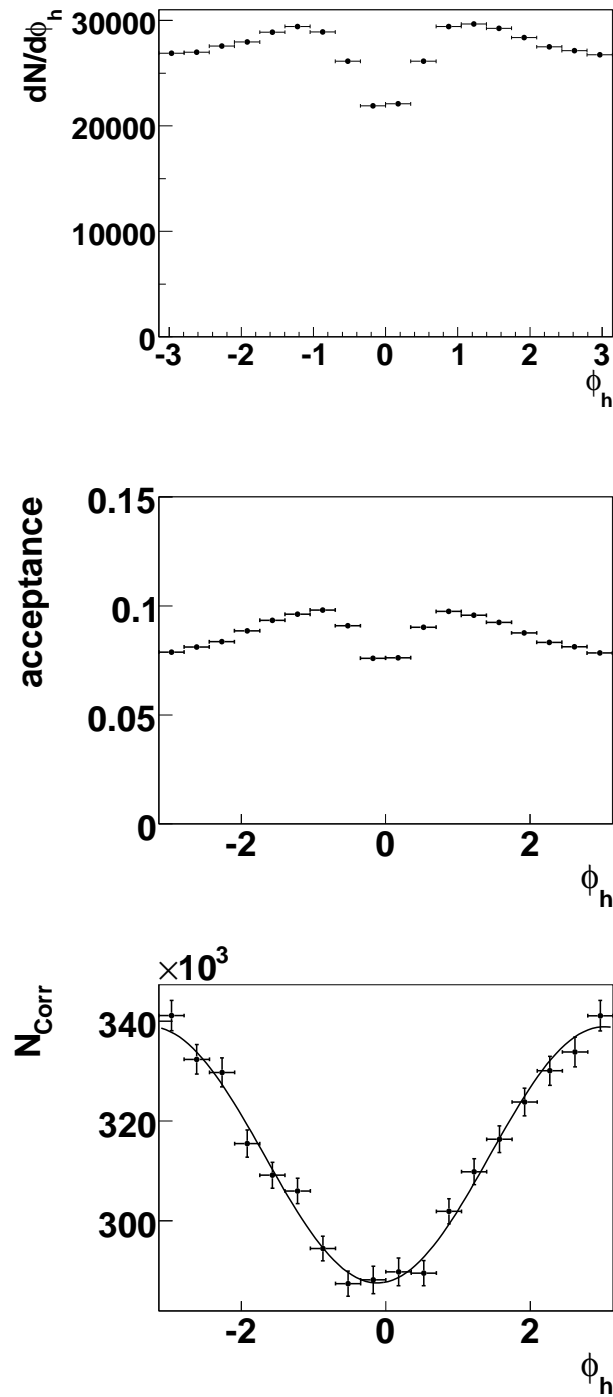


Figure 5.9: top: measured ϕ_h distribution in the upstream cell, middle: acceptance function for the upstream cell, bottom: corrected counting rate of the upstream cell with a fit according to Eq. 5.7.

6. Results

This chapter contains the results for the $\cos\phi_h$ and $\cos 2\phi_h$ moments. In Sec. 6.1 the dependency of the moments on x, y, Q^2, z_h and P_t^h is discussed. The $\cos\phi_h$ moment will be used to estimate the transverse momentum of the quarks k_t in Sec. 6.2. For the $\cos 2\phi_h$ asymmetry a model calculation [24] has been performed by V. Barone et al., taking into account Cahn, Boer-Mulders and QCD contributions. It will be compared to the measured moments in Sec. 6.3. This chapter concludes with the results of various systematic checks in Sec. 6.4.

6.1 Dependence on Kinematic Variables

This section shows the dependence of the cosine modulations on different kinematical variables for positive and negative hadrons. Although statistical errors are shown, they are often smaller than the markers. The plotted quantity is $A_{\cos\phi_h}$ or $A_{\cos 2\phi_h}$ respectively, as defined by Eq. 5.8, i.e. the moment divided by the corresponding y -dependent function given by Eq. 2.20 and Eq. 2.21. The observed $\cos\phi_h$ moment is of the order of 0.05-0.1, while the $\cos 2\phi_h$ moment is mostly smaller than 5%. In general, the results show a contradictory behavior. Some of the prediction based on Cahn and perturbative QCD are mirrored in the data, while others are not. The interpretation is complicated by the fact, that the kinematical variables measured in the COMPASS experiment are correlated. Although this is neglected in this analysis, this means that seemingly unexpected behavior in one variable can be caused by “hidden” dependencies on other variables. The results are charge dependent, which is quite surprising, since the QCD contribution is charge independent. The Cahn effect might depend, on the charge if the transverse momentum of up and down quarks is different. Since up quarks preferably fragment into positive and down quarks into negative pions, this might lead to a charge dependence in the observed moments. But, as will be shown in Sec. 6.2, the transverse momentum seems to be flavor independent. So it seems, that this effect cannot be explained within these models. The most promising ansatz might be a possible Boer-Mulders contribution to the $\cos\phi_h$ asymmetry. However, since a reliable estimate of a systematic error is still missing (see Sec. 6.4), a possible systematic effect cannot be ruled out.

In Fig. 6.1, the dependence of the moments on x is shown. Whereas the Cahn Effect alone is independent of x , the QCD contributions described in Sec. 2.5.3 do depend on x . The variations with x of the moments are rather strong, however this could also be due to correlations of x with other variables. Since the y dependence of the cross section has been factored out, no y dependence is expected. Indeed the results shown in Fig. 6.2 vary only weakly with y . For the Q^2 dependence, from the Cahn Effect

alone, a $1/\sqrt{Q^2}$ slope is expected for the $\cos\phi_h$ and a $1/Q^2$ dependence for the $\cos 2\phi_h$ amplitudes. As Fig. 6.3 shows, this is somewhat reproduced for $A_{\cos\phi_h}$, but not for $A_{\cos 2\phi_h}$.

Both the QCD and the Cahn contributions predict a z_h dependence for the moments and indeed the results depicted in Fig. 6.4 show a rather strong dependence on z_h . The cosine modulation does not change the sign for small z_h as would be expected, since the Cahn effect should vanish there and the QCD contributions for small z_h are expected to give rise to a positive asymmetry. From the pure Cahn effect, which should dominate especially for the leading hadron case, a linear z_h dependence is expected. This is reproduced by the leading hadron sample as well as for the all hadron sample for $z_h \gtrsim 0.25$.

The Cahn Effect alone also predicts a linear dependence in P_t^h for the $\cos\phi_h$ moment, however the QCD contributions get increasingly important with higher P_t^h , leading to deviations from the linearity. As depicted in Fig. 6.5, the $\cos\phi_h$ moment for the leading hadron shows a linear dependence on P_t^h , showing no evidence for deviations from the linearity at $P_t^h \gtrsim 1$ GeV.

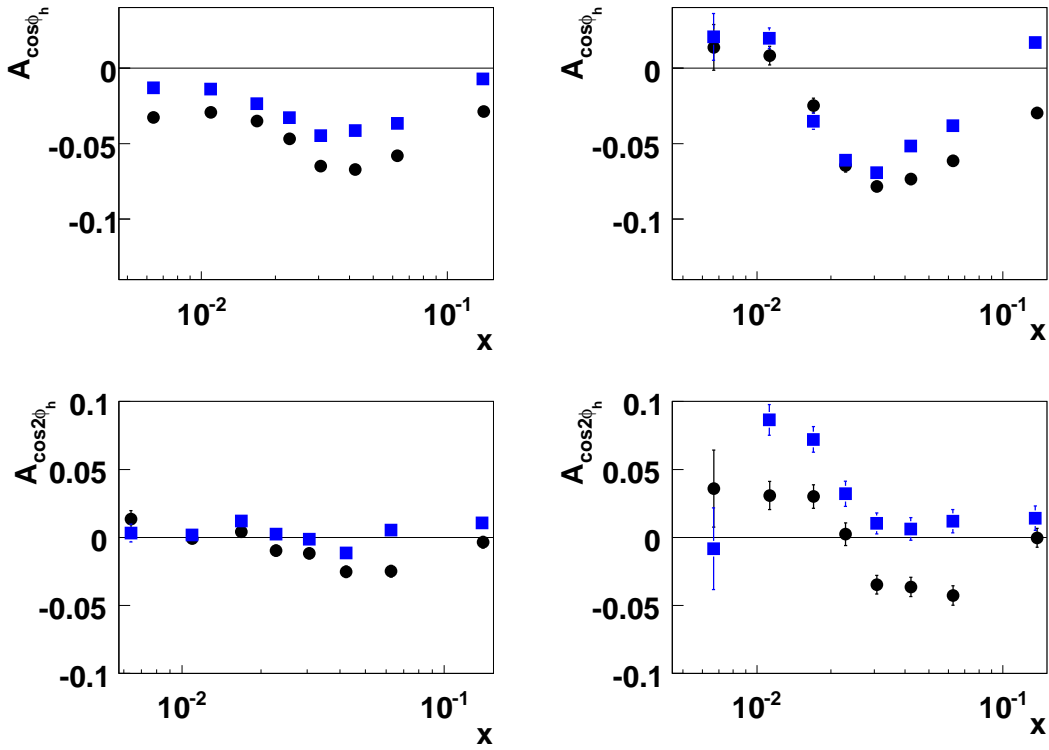


Figure 6.1: The observed $\cos\phi_h$ (upper row) and $\cos 2\phi_h$ (lower row) modulations binned in x . The plots on the left hand side show the results for all hadrons and the ones on right hand side the leading hadron results. The black dots indicate the results for positive, the blue squares the results for negative hadrons.

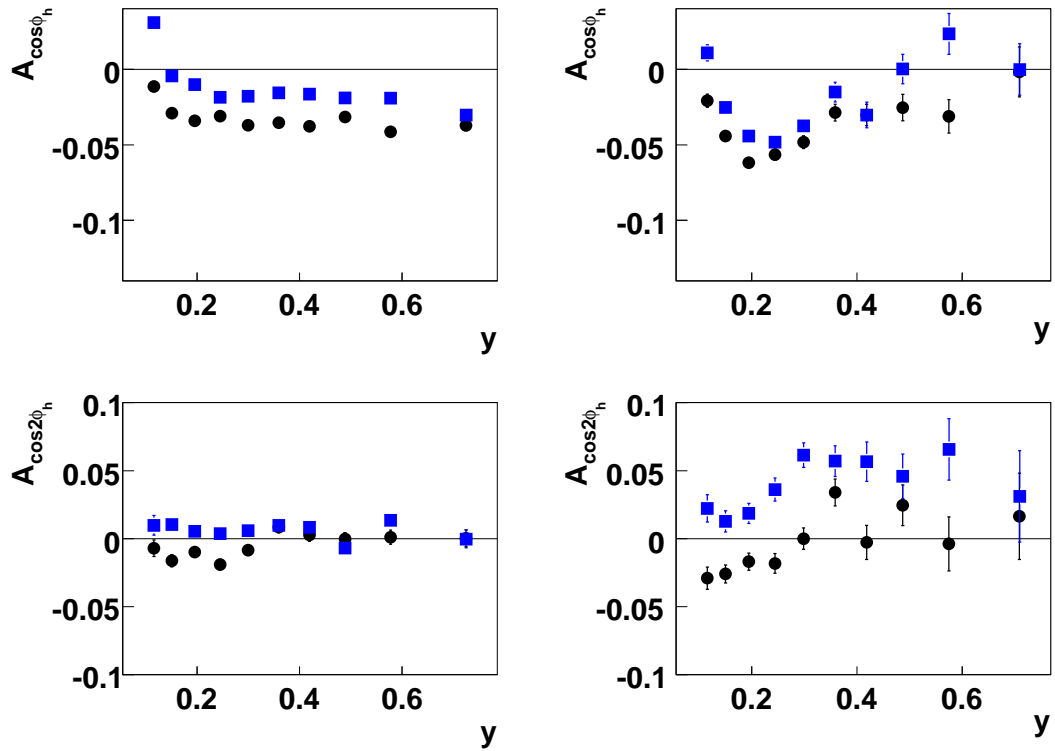


Figure 6.2: $\cos\phi_h$ (upper row) and $\cos 2\phi_h$ modulations (lower row) binned in y , again the all hadron sample on the left, the leading hadrons on the right and black dots for positive and blue squares for negative hadrons.

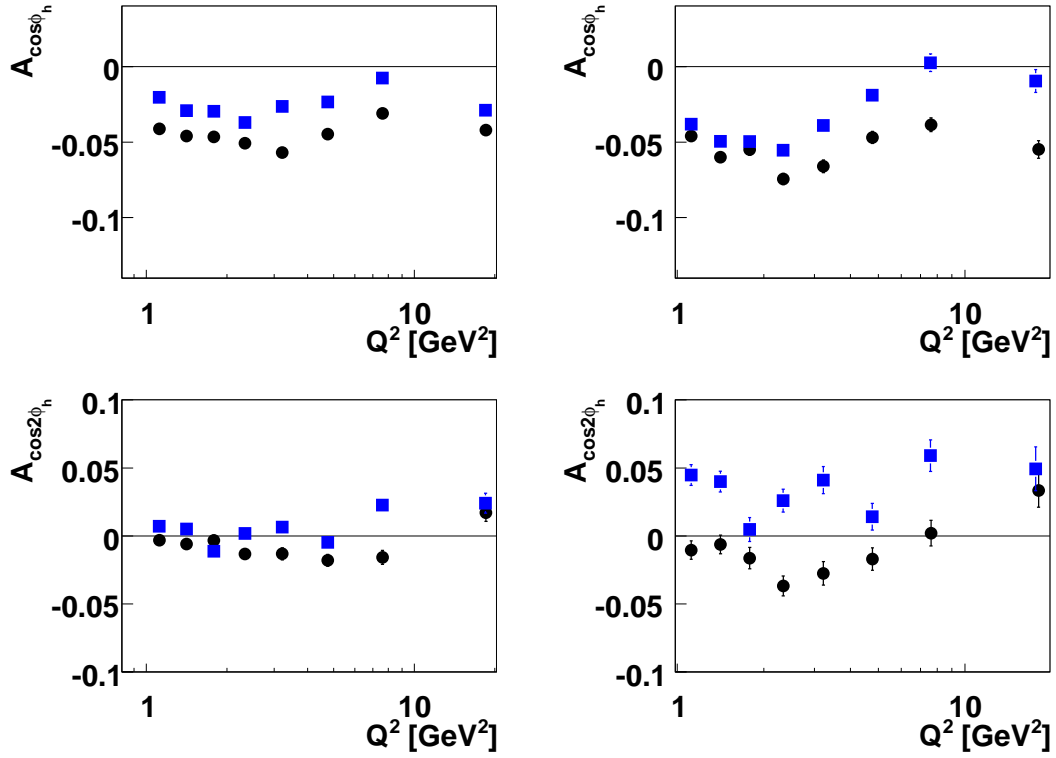


Figure 6.3: Results for Q^2 binning, $\cos\phi_h$ (upper row) and $\cos 2\phi_h$ modulations (lower row) for all hadrons (left) and leading hadrons (right) for positive (black dots) and negative (blue squares) hadrons.

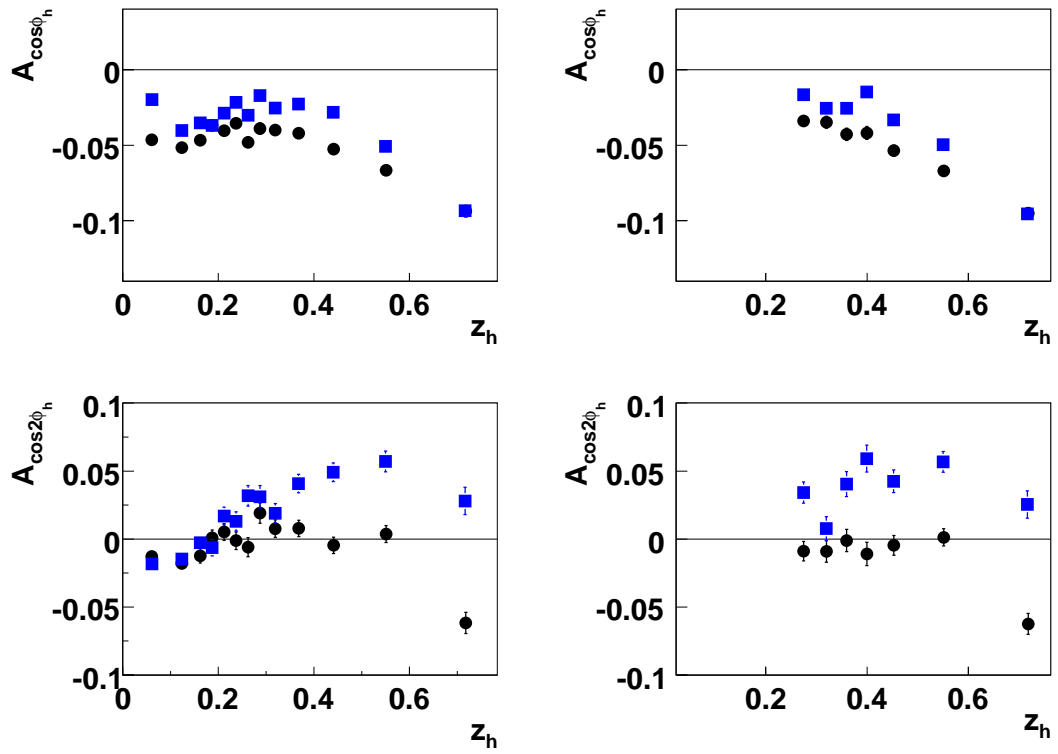


Figure 6.4: z_h binning, as usual $A_{\cos\phi_h}$ in the upper row and $A_{\cos 2\phi_h}$ in the lower row for all (left) and leading hadrons (right) for positive (black dots) and negative (blue squares) hadrons.

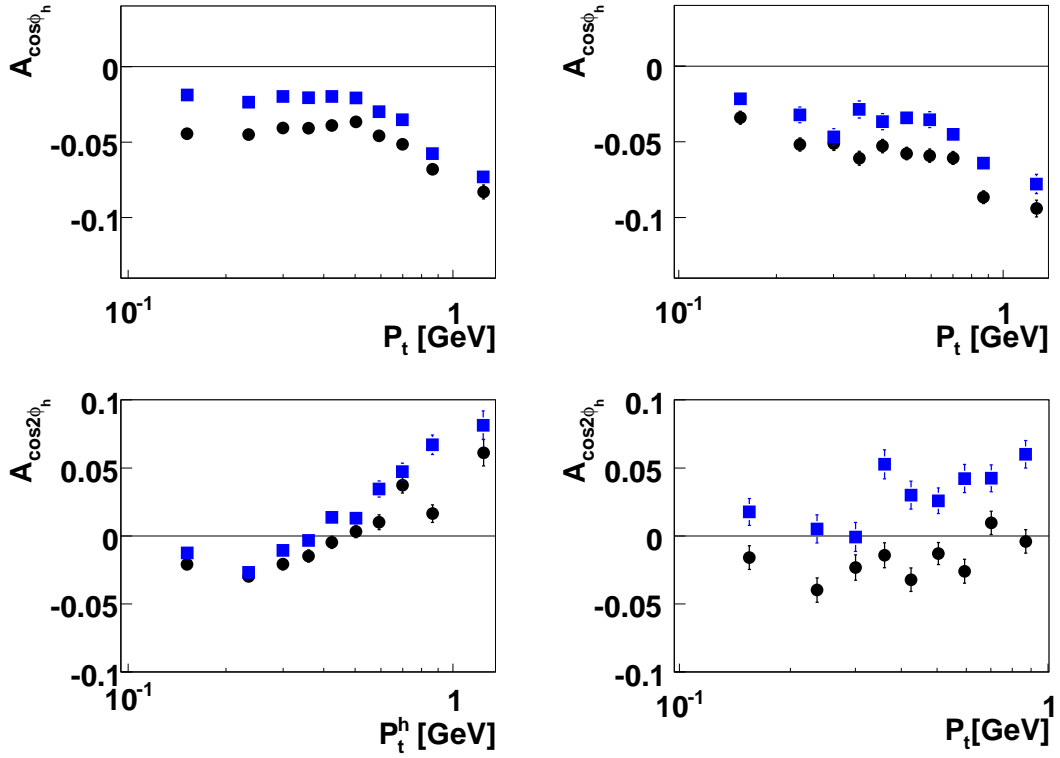


Figure 6.5: The observed $\cos\phi_h$ and $\cos2\phi_h$ modulations binned in P_t^h , $A_{\cos\phi_h}$ in the upper row and $A_{\cos2\phi_h}$ in the lower row for all (left) and leading hadrons (right) for positive (black dots) and negative (blue squares) hadrons.

6.2 The $\cos \phi_h$ Moment - the Transverse Momentum of the Quarks

Disentangling the different sources for azimuthal modulations described in Sec. 2.5 would go beyond this thesis. However, since the dominant contribution for the $\cos \phi_h$ modulation is caused by the transverse momentum of the quarks, one can try to neglect all other terms. This is especially true for the leading hadron sample, since it is enriched with hadrons containing the struck quark. As already mentioned in 2.5.1, in this case the cross section can be written as

$$\frac{d^5\sigma}{dx dy dz_h P_t^h dP_t^h d\phi_h} \propto \sum_q \exp\left(-\frac{(P_t^h)^2}{\langle(P_t^h)^2\rangle}\right) f_q(x) D_q^h(z_h) (1 + (1 - y^2)) \cdot \left[1 - 4D_{\cos \phi_h}(y) \frac{\langle k_t^2 \rangle z_h P_t^h}{Q \langle(P_t^h)^2\rangle} \cos \phi_h\right]. \quad (6.1)$$

In this simple model $\langle \cos \phi_h \rangle$ should be linear in z_h and P_t^h after integrating over all other variables:

$$\langle \cos \phi_h \rangle = -2 \left\langle \frac{D_{\cos \phi_h}(y) P_t^h}{Q} \right\rangle \frac{\langle k_t^2 \rangle}{\langle(P_t^h)^2\rangle} z_h, \quad (6.2)$$

$$\langle \cos \phi_h \rangle = -2 \left\langle \frac{D_{\cos \phi_h}(y) z_h}{Q} \right\rangle \frac{\langle k_t^2 \rangle}{\langle(P_t^h)^2\rangle} P_t^h. \quad (6.3)$$

The mean transverse momentum can then be determined from the slope. The obtained $\cos \phi_h$ moments in dependence of z_h and P_t^h , are shown together with a linear fit in Fig. 6.6. Although no constant term should be present, the constant differs significantly from zero in all fits. The factors needed to obtain the transverse momentum from the slopes are given by $\left\langle \frac{D_{\cos \phi_h}(y) P_t^h}{Q} \right\rangle = 0.35$, $\left\langle \frac{D_{\cos \phi_h}(y) z_h}{Q} \right\rangle = 0.27 \text{ GeV}^{-1}$ and $\langle(P_t^h)^2\rangle = 0.4 \text{ GeV}^2$. Alternatively, the mean transverse momentum can be determined by integrating over the complete kinematic range of the leading hadron sample:

$$\langle \cos \phi_h \rangle = -2 \left\langle \frac{D_{\cos \phi_h}(y) P_t^h z_h}{Q} \right\rangle \frac{\langle k_t^2 \rangle}{\langle(P_t^h)^2\rangle}. \quad (6.4)$$

Here the multiplicative factor needed to obtain $\langle k_t^2 \rangle$ is $\left\langle \frac{D_{\cos \phi_h}(y) P_t^h z}{Q} \right\rangle = 0.15$.

The results for the three methods are listed in Tbl. 6.1. The P_t^h method is not in agreement within the others, but at least agrees in the order of magnitude. A model calculation including Cahn and QCD effects with a similar value of $\langle k_t^2 \rangle = 0.25 \text{ GeV}^2$ has been published in [17] together with a comparison with EMC data. The results do not depend on the charge of the hadron, so there is no evidence, that the transverse momentum differs for up and down quarks.

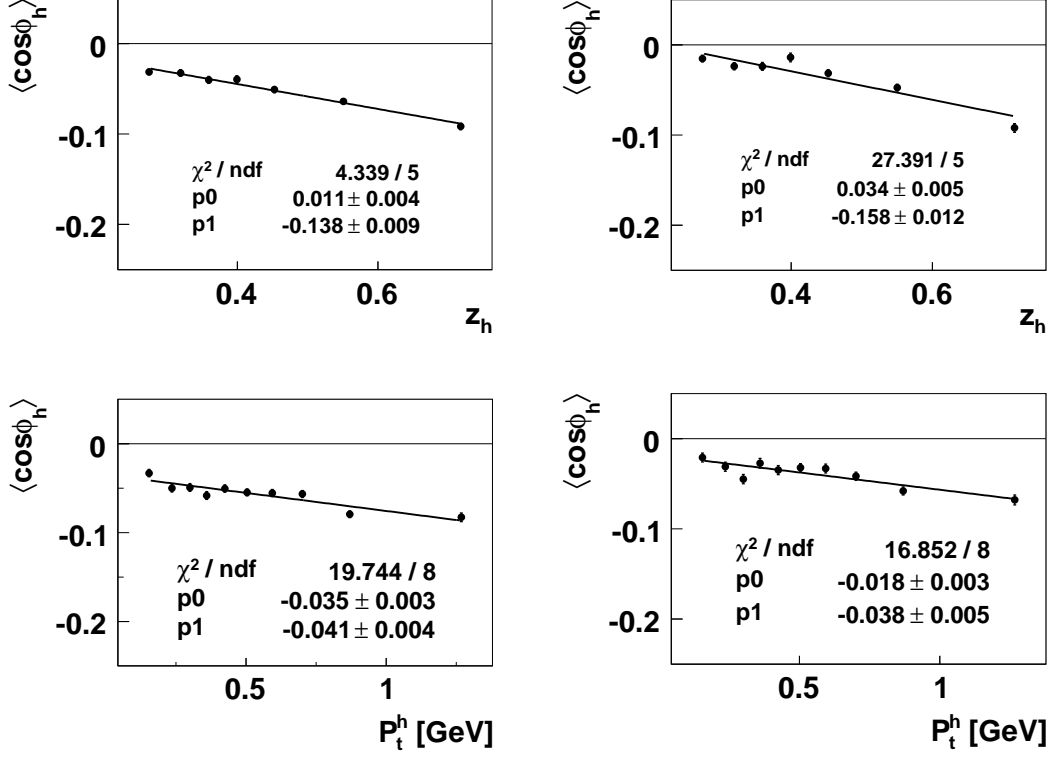


Figure 6.6: The moments $\langle \cos \phi_h \rangle$ binned in z_h and P_t^h and fitted with a linear function: $\langle \cos \phi_h \rangle = p0 + p1 z_h (P_t^h)$.

Table 6.1: transverse momentum of the quarks $\langle k_t^2 \rangle$

method	$\langle k_t^2 \rangle$ [GeV ²]	$\sigma_{\langle k_t^2 \rangle}$ [GeV ²]
all leading hadron data, positive hadrons	0.08	0.01
all leading hadron data, negative hadrons	0.07	0.01
z_h dependence, positive hadrons	0.079	0.005
z_h dependence, negative hadrons	0.090	0.006
P_t^h dependence, negative hadrons	0.029	0.004
P_t^h dependence, positive hadrons	0.030	0.003

6.3 The $\cos 2\phi_h$ Moment - Comparison with Theory

Recently a calculation by V. Barone et al. has been performed [23, 24]. It includes both Cahn and Boer-Mulders contributions as well as QCD effects. However, since the Boer-Mulders Function is essentially unmeasured, they assumed $h_1^\perp \propto f_{1T}$, where f_{1T} is the Siverson function. This assumption has been motivated in [51], and the proportionality constants, given for the deuteron by

$$h_1^{\perp u} \simeq 1.80 f_{1T}^{\perp u} \quad \text{and} \quad h_1^{\perp d} = -0.94 f_{1T}^{\perp d}, \quad (6.5)$$

have been obtained from lattice QCD calculations published in [52]. The Siverson Function f_{1T} describes the probability to find an unpolarized quark in a transversely polarized nucleon and can be measured in SIDIS with a transversely polarized target, where it gives rise to the Siverson effect [53]. The parameterizations used for the predictions are taken from [54] for the Siverson Function and from [55] for the Collins fragmentation function. The predictions as well as the measured values for the $\cos 2\phi_h$ moments are depicted in Fig. 6.7 in dependence of x and z_h and for different lower cuts P_t^{CUT} on P_t^h , each time integrating over the remaining P_t^h range.

Since for the predictions a cut on $z_h > 0.2$ was applied, this was also done for the comparison with x and P_t^{CUT} . Otherwise the applied cuts are identical to the ones for the all hadron sample described in chapter 4. Considering that neither the proportionality of h_1^\perp to f_{1T} nor the proportionality factors themselves have been experimentally tested, the agreement is encouraging, although for positive hadrons the dependence on x of the data disagrees with the prediction also in the sign. The observed moments are in all cases smaller than the predicted ones, but the order of magnitude is correct.

6.4 Systematic Checks

The first step is to see whether the fitted function Eq. 5.7 describes the corrected count rates. A measure for this is the χ_{red}^2 -distribution of the fits, which is shown exemplarily for the all hadron sample together with the expected distribution

$$f(\chi_{\text{red}}^2, k = 14) \propto (kx)^{-k/2} \exp -kx/2 \quad (6.6)$$

in Fig.6.8. The degree of freedom k in this case is 14 (18 bins minus 4 parameters). Since the χ_{red}^2 -distribution is well reproduced by the χ_{red}^2 of the fits, the data seems to be well described by Eq. 5.7.

Additional checks can be done by comparing results for different positions of the primary vertex. The analysis was done for upstream and downstream cell separately. This allows to determine whether the detector description in the MC works properly by comparing the results for the two cells. In this context, it is useful to define a quantity called Pull as follows:

$$\text{Pull} = \frac{A_1 - A_2}{\sqrt{\sigma_1^2 + \sigma_2^2}} \quad (6.7)$$

where $A_{1(2)}$ are the results for upstream and downstream cell in a given kinematic bin and $\sigma_{1(2)}$ their respective (statistical) errors. Since the physics should in principle be

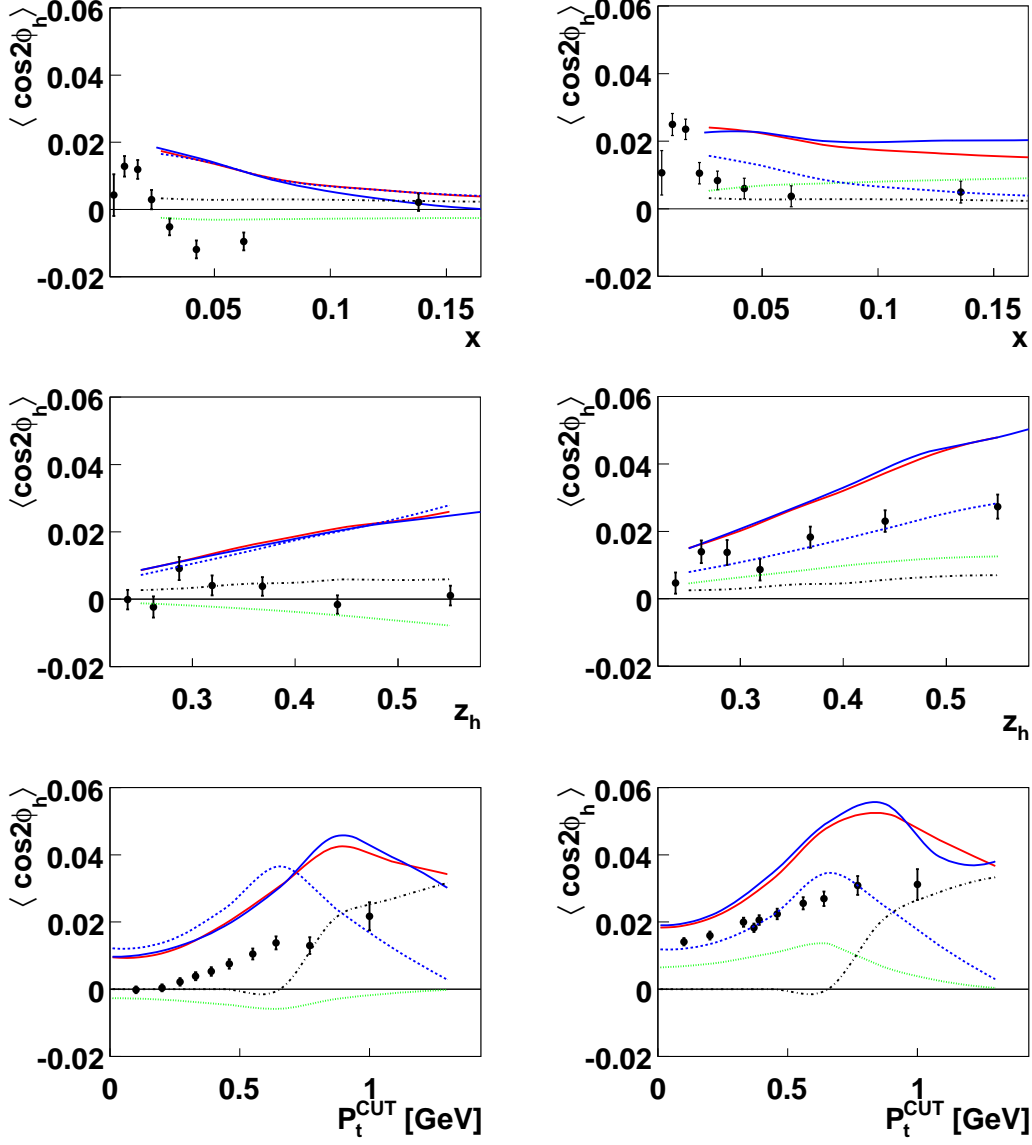


Figure 6.7: Comparison of the $\cos 2\phi_h$ asymmetries with the predictions in [24] in x , z_h and P_t^{CUT} . The green dotted line describes the Boer-Mulders contribution for a proton target. The blue dashed line the Cahn effect and the black dashed-dotted line perturbative QCD contributions. The red line corresponds to the sum of these three and describes the $\cos 2\phi_h$ asymmetry for the proton and the blue line describes the full asymmetry for the deuteron. The left plots are for positive, the right for negative hadrons.

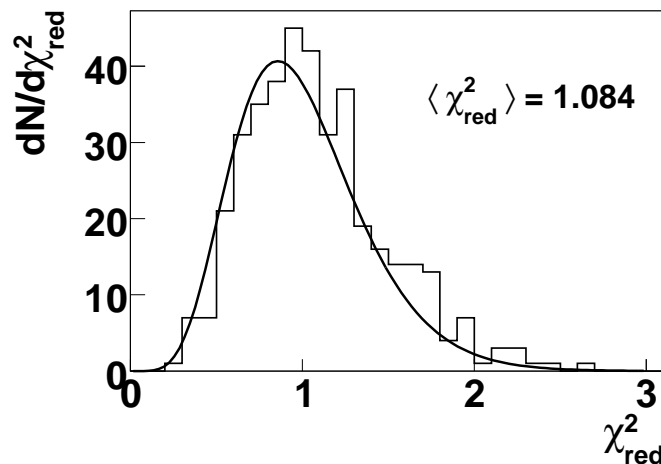


Figure 6.8: The χ^2_{red} -distribution of the fits of the all hadron sample. The curve shows a fit with the expected distribution, where the amplitude is the only free parameter.

independent of the target cell, the mean value $\langle \text{Pull} \rangle$ of all Pulls should be compatible with zero and the RMS error σ_{Pull} compatible with one.

However, the two cells cover slightly different kinematic regions mostly due to the larger angular acceptance of the downstream cell, so some difference is expected. Similar tests can be done by splitting the data further, e.g. only the data where the primary vertex is in the upper part of the downstream target cell is used and divided into a left and right part. From the results of these two parts an analogously defined Pull can be obtained. These checks have been done on the all hadron sample, since this sample has an extremely small statistical error and is thus much more sensitive to systematic effects than the leading hadron sample. The mean value and the RMS errors of these tests are summarized in Tbl. 6.2. In general the left-right comparisons give significantly better results than the up-down ones. The reason for this behavior might be a difference in the description of the target density between data and MC simulation. In reality, the target material tends to settle down, so the target density is a function of the Y -coordinate, a fact which is not included in the detector simulation. This may lead to an additional Y -dependence of the results, since this mismatch in the target density causes a difference in the vertex distribution and the acceptance depends on the vertex position. Also it is known, that electron contamination is different for upper and lower part of the target [56]. This might also contribute to this effect.

Another possible source of systematic errors would be variations in the detector performance. The stability of the spectrometer was checked by building the ratio of the ϕ_h distributions of week 26 and week 27 and fitting it with Eq. 5.7. As can be seen in Fig. 6.9, the ratio is almost flat and all amplitudes compatible with zero. Additionally, also the ratio of the kinematic distributions was checked and found to be compatible

Table 6.2: $\langle \text{Pull} \rangle$ and σ_{Pull} for several systematic checks

Test	$A_{\cos \phi_h}$		$A_{\cos 2\phi_h}$	
	$\langle \text{Pull} \rangle$	σ_{Pull}	$\langle \text{Pull} \rangle$	σ_{Pull}
Upstream vs downstream cell	-0.58 ± 0.10	1.65 ± 0.08	0.18 ± 0.08	1.22 ± 0.06
Upstream cell				
top: left vs right	0.12 ± 0.06	0.97 ± 0.05	-0.01 ± 0.08	1.07 ± 0.08
bottom: left vs right	0.12 ± 0.06	0.97 ± 0.05	0.27 ± 0.07	1.01 ± 0.05
left: top vs bottom	0.65 ± 0.07	0.97 ± 0.05	-0.36 ± 0.06	0.87 ± 0.04
right: top vs bottom	-0.38 ± 0.07	0.95 ± 0.05	-0.18 ± 0.08	1.02 ± 0.05
Downstream cell				
top: left vs right	-0.08 ± 0.07	1.01 ± 0.05	0.02 ± 0.06	0.88 ± 0.04
bottom: left vs right	-0.15 ± 0.07	0.97 ± 0.05	-0.19 ± 0.07	0.97 ± 0.05
right: top vs bottom	-0.46 ± 0.08	1.08 ± 0.05	0.02 ± 0.07	0.94 ± 0.05
left: top vs bottom	-0.38 ± 0.07	1.03 ± 0.05	-0.10 ± 0.06	0.91 ± 0.05

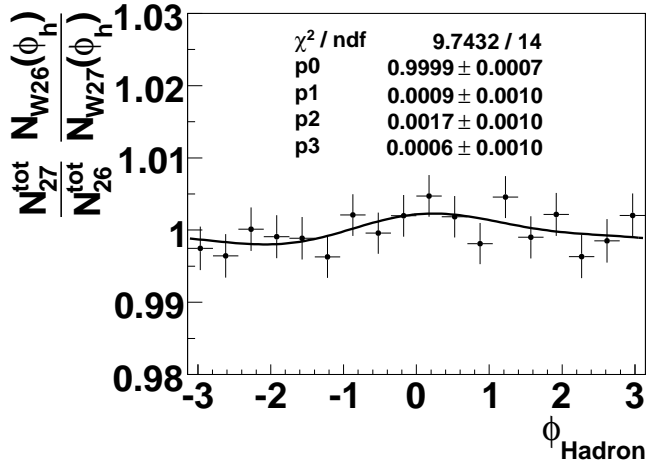


Figure 6.9: The ratio of the periods W26 and W27, scaled to equal number of hadrons and fitted with Eq. 5.7. Since all amplitudes are compatible with zero, there is no significant contribution of the stability of the apparatus to the systematic error.

with a constant, all leading to the conclusion that time-dependent effects are negligible for these two periods.

The influence of polarization effects can be estimated by comparing the ϕ_h distributions measured in the two polarization configurations. Again, the ratio is compatible with a constant, since all fitted amplitudes are compatible with zero.

While the contributions of the data to a systematic error seems to be small, there are clear indications of systematic effects, which have their origin in effects not properly described in the MC simulation. They seem to be slightly larger than the statistical error, but more work is needed to gain a reliable estimate of a systematic error.

7. Summary and Outlook

The aim of this thesis was to investigate the dependence of the SIDIS cross section on the hadron azimuthal angle ϕ_h based on data taken at the COMPASS experiment in 2004. For this, a MC simulation was performed to correct the measured count rates for modulations caused by the non-uniform detector acceptance. From these corrected count rates, the modulations of the cross section have been extracted.

There are three different effects which cause dependencies of the cross section on the azimuthal angle ϕ_h :

- The Cahn effect: A pure leading order QED effect due to the transverse momentum of the quarks.
- Perturbative QCD.
- Spin and transverse momentum dependent PDFs, in particular the Boer-Mulders contribution to the $\cos 2\phi_h$ asymmetry.

These effects lead to a dependence of the cross section on $\cos \phi_h$ and $\cos 2\phi_h$. An additional $\sin \phi_h$ dependence exists, since the COMPASS experiment measures with a polarized beam. Since azimuthal modulations are also introduced by the acceptance of the COMPASS spectrometer, a MC simulation has been carried out to correct for this systematic effect. Although the quality of the MC description is still satisfactory, it is presently the main limitation to enhance the precision of the determination of these moments. Various tests have been performed to understand the shape of the acceptance and to check the acceptance correction. There are signs of systematic problems, but they seem to be under control.

In this thesis, the $\cos \phi_h$, $\cos 2\phi_h$ and $\sin \phi_h$ moments were determined in dependence on x, y, Q^2, z_h and P_t^h . The analysis was performed both for a sample containing all charged hadrons and on a subsample consisting of the hadrons with the largest energy fraction z_h . The leading hadron sample allows to estimate the mean transverse momentum of the quarks $\langle k_t^2 \rangle$, since leading hadrons have a higher likelihood to contain the struck quark and thus the Cahn effect should be enhanced compared to the other two contributions. In this case, the cross section can be simplified by taking only into account the $\cos \phi_h$ term of the Cahn effect and neglecting the other terms. With this approach, a rough estimate of the mean quark transverse momentum $\langle k_t^2 \rangle \approx 0.1 \text{ GeV}^2$ has been obtained from the $\cos \phi_h$ moments. This model turned out to be insufficient to describe all the observed kinematical dependencies. Nevertheless, the estimate agrees in the order of magnitude with the results of previous publications. The results for

the $\cos 2\phi_h$ moments were compared to a recent model calculation by V. Barone et al. Considering that the predictions rely on several assumptions which have never been experimentally tested, the agreement is encouraging. The results of this thesis should allow to develop more refined models. Some of the discrepancies might be due to correlations between the measured kinematic variables, which were not taken into account in the model. Therefore it might be interesting to try to determine the moments with a multidimensional kinematic binning. This would allow to determine the correlations, but it has to be seen whether the statistics is sufficient. Also, more work is needed to arrive at a precise estimate of the systematic error. In particular, it will be interesting to compare the results of this thesis with the results obtained from transverse data. Additionally, more MC simulations should be performed, using different parameters for the generator and the detector simulation to study the effect of these parameters on the acceptance correction. It might also be interesting, to include the Cahn effect in the MC generation and determine k_t^2 by inserting different values of $\langle k_t^2 \rangle$ in the MC simulation and compare the obtained ϕ_h distributions with the measured one.

A. Appendix

A.1 The $\sin \phi_h$ moment

This section contains the results for the $\sin \phi_h$ moment. The moment is divided through the average values of the beam polarization $\langle P_b \rangle = 0.8$ and the kinematic factor $D_{\sin \phi_h}$ defined in Eq. 2.29:

$$A_{\sin \phi_h} = \frac{\langle \sin \phi_h \rangle}{\langle D_{\sin \phi_h} \rangle \langle P_b \rangle}. \quad (\text{A.1})$$

Polarization effects are best measured in experiments which are able to measure with both beam polarizations, which gives a better handle on systematic effects. Such measurements have been performed by the CLAS collaboration [57], reporting an average value of $0.038 \pm 0.005 \pm 0.003$. This seems to be in agreement with the values measured here.

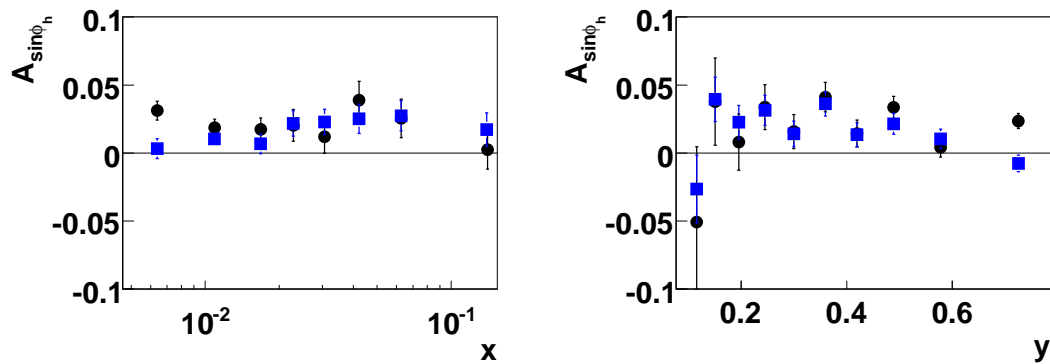


Figure A.1: The observed $\sin \phi_h$ modulations for the all hadron sample binned in x and y . The black dots indicate the results for positive, the blue squares the results for negative hadrons.

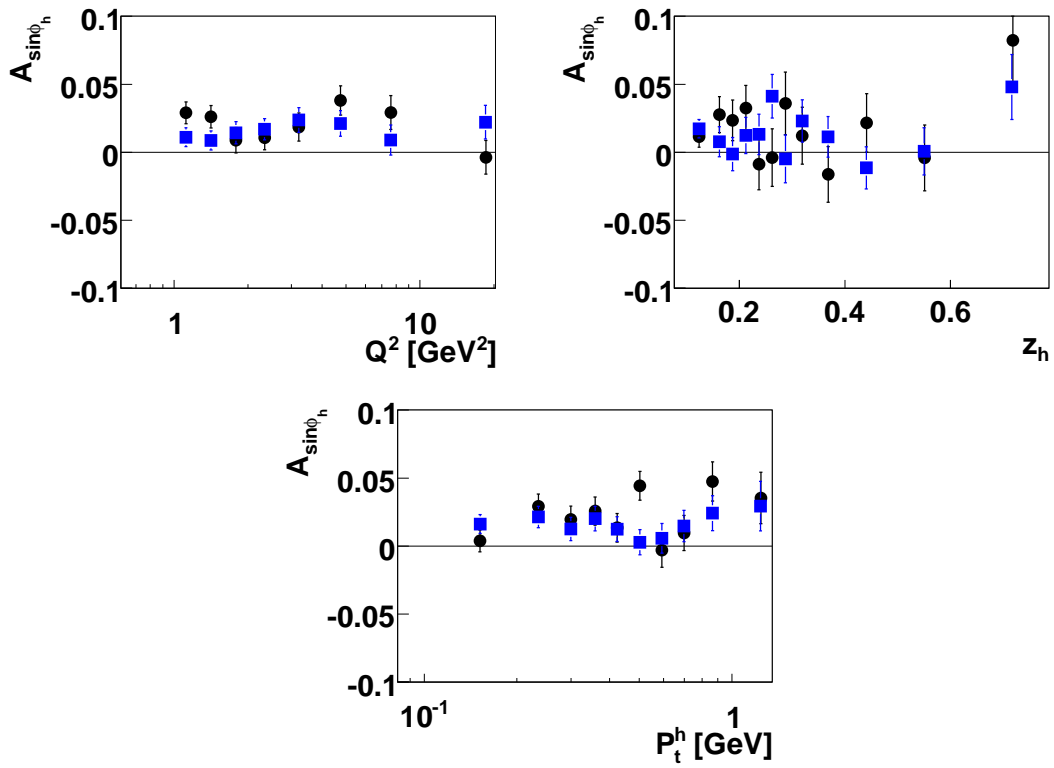


Figure A.2: The observed $\sin \phi_h$ modulations for the all hadron sample binned in Q^2 , z_h and P_t^h for positive (black dots) and negative (blue squares) hadrons.

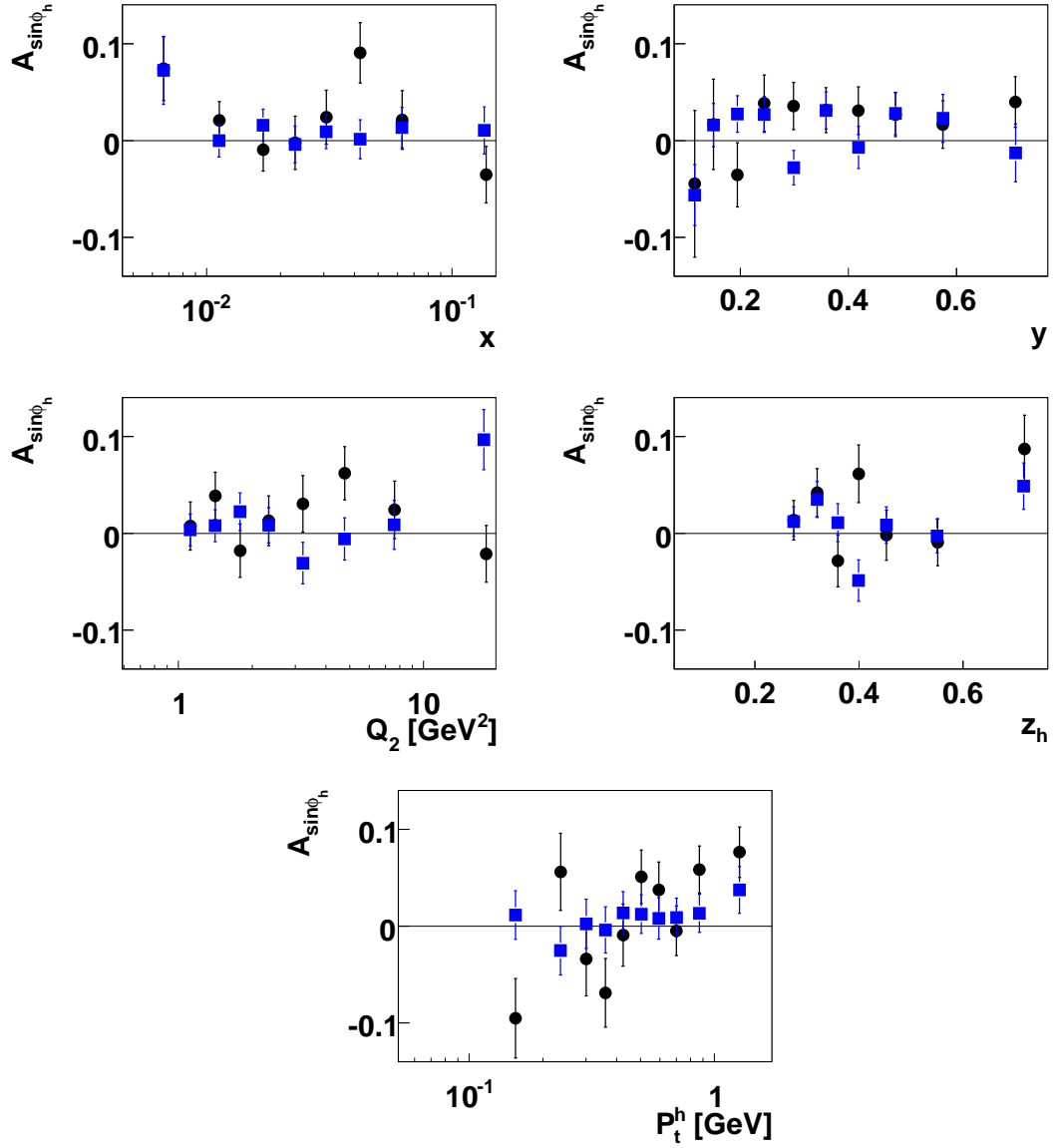


Figure A.3: The observed $\sin \phi_h$ modulations for the leading hadron sample binned in x, y, Q^2, z_h and P_t^h . Again, the black dots indicate the results for positive, the blue squares the results for negative hadrons.

A.2 Tables

Table A.1: Parameters for Particle Identification

	$C_{2\text{ndmax}}$	C_{BG}	approx. P_{min} [GeV]	max. momentum [GeV]
Pion	1.05	1.05	3	43
Kaon	1.05	1.05	9	43
Proton	1.05	1.05	18	43
Electron	1.5	1.5		8

Table A.2: Binning

x	y	$Q^2[\text{GeV}^2]$	z_h	$P_t^h[\text{GeV}]$
$0 < x < 0.008$	$0.1 < y < 0.13$	$1.0 < Q^2 < 1.25$	$0.0 < z_h < 0.1$	$0.1 < P_t^h > 0.2$
$0.008 < x < 0.014$	$0.13 < y < 0.17$	$1.25 < Q^2 < 1.6$	$0.1 < z_h < 0.15$	$0.2 < P_t^h > 0.27$
$0.014 < x < 0.02$	$0.17 < y < 0.22$	$1.6 < Q^2 < 2.0$	$0.15 < z_h < 0.155$	$0.27 < P_t^h > 0.33$
$0.02 < x < 0.026$	$0.22 < y < 0.27$	$2.0 < Q^2 < 2.75$	$0.175 < z_h < 0.2$	$0.33 < P_t^h > 0.39$
$0.026 < x < 0.036$	$0.27 < y < 0.33$	$2.75 < Q^2 < 3.8$	$0.2 < z_h < 0.225$	$0.39 < P_t^h > 0.46$
$0.036 < x < 0.05$	$0.33 < y < 0.39$	$3.8 < Q^2 < 6.0$	$0.225 < z_h < 0.25$	$0.46 < P_t^h > 0.55$
$0.05 < x < 0.08$	$0.39 < y < 0.45$	$6.0 < Q^2 < 10.0$	$0.25 < z_h < 0.275$	$0.55 < P_t^h > 0.64$
$0.08 < x < 1.0$	$0.45 < y < 0.53$	$10.0 < Q^2$	$0.275 < z_h < 0.3$	$0.64 < P_t^h > 0.77$
	$0.53 < y < 0.63$		$0.3 < z_h < 0.34$	$1.1 < P_t^h$
	$0.63 < y < 0.85$		$0.34 < z_h < 0.4$	
			$0.4 < z_h < 0.49$	
			$0.49 < z_h < 0.63$	
			$0.63 < z_h < 0.85$	

Table A.3: results for the all hadron sample, positive hadrons, binned in x

$\langle x \rangle$	$A_{\cos \phi_h}$	$\sigma_{A_{\cos \phi_h}}$	$A_{\cos 2\phi_h}$	$\sigma_{A_{\cos 2\phi_h}}$
0.0064	-0.0330	0.0032	0.0134	0.0063
0.011	-0.0293	0.0016	-0.0008	0.0034
0.017	-0.0350	0.0017	0.0042	0.0036
0.023	-0.0465	0.0020	-0.0097	0.0041
0.031	-0.0655	0.0019	-0.0118	0.0038
0.042	-0.0675	0.0021	-0.0253	0.0042
0.063	-0.0585	0.0021	-0.0249	0.0043
0.141	-0.0284	0.0022	-0.0036	0.0043

Table A.4: results for the all hadron sample, negative hadrons, binned in x

$\langle x \rangle$	$A_{\cos \phi_h}$	$\sigma_{A_{\cos \phi_h}}$	$A_{\cos 2\phi_h}$	$\sigma_{A_{\cos 2\phi_h}}$
0.0064	-0.0124	0.0028	0.0032	0.0065
0.011	-0.0141	0.0017	0.0018	0.0036
0.017	-0.0235	0.0019	0.0122	0.0038
0.023	-0.0329	0.0022	0.0024	0.0044
0.031	-0.0440	0.0020	-0.0013	0.0041
0.042	-0.0406	0.0023	-0.0114	0.0047
0.063	-0.0366	0.0024	0.0053	0.0048
0.139	-0.0074	0.0025	0.0107	0.0050

Table A.5: results for the all hadron sample, positive hadrons, binned in Q^2

$\langle Q^2 \rangle [\text{GeV}^2]$	$A_{\cos \phi_h}$	$\sigma_{A_{\cos \phi_h}}$	$A_{\cos 2\phi_h}$	$\sigma_{A_{\cos 2\phi_h}}$
1.1	-0.0411	0.0016	-0.0033	0.0033
1.4	-0.0460	0.0016	-0.0067	0.0034
1.8	-0.0470	0.0019	-0.0032	0.0039
2.3	-0.0510	0.0018	-0.0133	0.0037
3.2	-0.0565	0.0021	-0.0129	0.0045
4.8	-0.0449	0.0021	-0.0170	0.0044
7.6	-0.0312	0.0024	-0.0137	0.0051
18.5	-0.0419	0.0030	0.0170	0.0064

Table A.6: results for the all hadron sample, negative hadrons, binned in Q^2

$\langle Q^2 \rangle [\text{GeV}^2]$	$A_{\cos \phi_h}$	$\sigma_{A_{\cos \phi_h}}$	$A_{\cos 2\phi_h}$	$\sigma_{A_{\cos 2\phi_h}}$
1.1	-0.0204	0.0017	0.0063	0.0036
1.4	-0.0288	0.0017	0.0050	0.0036
1.8	-0.0295	0.0020	-0.0112	0.0042
2.3	-0.0370	0.0019	0.0001	0.0041
3.2	-0.0259	0.0023	0.0071	0.0048
4.8	-0.0226	0.0023	-0.0042	0.0048
7.6	-0.0079	0.0028	0.0227	0.0057
18.5	-0.0289	0.0034	0.0228	0.0073

Table A.7: results for the all hadron sample, positive hadrons, binned in y

$\langle y \rangle$	$A_{\cos \phi_h}$	$\sigma_{A_{\cos \phi_h}}$	$A_{\cos 2\phi_h}$	$\sigma_{A_{\cos 2\phi_h}}$
0.12	-0.0113	0.0033	-0.0058	0.0061
0.15	-0.0300	0.0024	-0.0157	0.0045
0.20	-0.0336	0.0020	-0.0093	0.0039
0.25	-0.0312	0.0020	-0.0202	0.0040
0.30	-0.0370	0.0019	-0.0084	0.0038
0.36	-0.0355	0.0021	0.0086	0.0042
0.42	-0.0372	0.0023	0.0036	0.0046
0.49	-0.0319	0.0022	-0.0007	0.0046
0.58	-0.0409	0.0024	0.0020	0.0052
0.73	-0.0378	0.0025	0.00040	0.0062

Table A.8: results for the all hadron sample, negative hadrons, binned in y

$\langle y \rangle$	$A_{\cos \phi_h}$	$\sigma_{A_{\cos \phi_h}}$	$A_{\cos 2\phi_h}$	$\sigma_{A_{\cos 2\phi_h}}$
0.12	0.0305	0.0039	0.0101	0.0072
0.15	-0.0050	0.0027	0.0101	0.0052
0.20	-0.0098	0.0022	0.0042	0.0043
0.25	-0.0188	0.0022	0.0033	0.0043
0.30	-0.0173	0.0021	0.0058	0.0041
0.36	-0.0158	0.0022	0.0087	0.0044
0.42	-0.0161	0.0024	0.0079	0.0049
0.49	-0.0188	0.0023	-0.0077	0.0048
0.58	-0.0187	0.0025	0.0161	0.0054
0.73	-0.0298	0.0026	-0.0007	0.0065

Table A.9: results for the all hadron sample, positive hadrons, binned in z_h

$\langle z_h \rangle$	$A_{\cos \phi_h}$	$\sigma_{A_{\cos \phi_h}}$	$A_{\cos 2\phi_h}$	$\sigma_{A_{\cos 2\phi_h}}$
0.061	-0.0465	0.0013	-0.0128	0.0028
0.12	-0.0517	0.0016	-0.0181	0.0034
0.16	-0.0475	0.0025	-0.0113	0.0053
0.19	-0.0365	0.0028	0.0017	0.0057
0.21	-0.0414	0.0030	0.0044	0.0061
0.24	-0.0348	0.0032	-0.0002	0.0065
0.26	-0.0473	0.0034	-0.0051	0.0070
0.29	-0.0383	0.0037	0.0198	0.0075
0.32	-0.0393	0.0032	0.0089	0.0064
0.37	-0.0418	0.0030	0.0082	0.0060
0.44	-0.0531	0.0029	-0.0034	0.0059
0.55	-0.0673	0.0031	0.0023	0.0062
0.72	-0.0940	0.0030	-0.0621	0.0077

Table A.10: results for the all hadron sample, negative hadrons, binned in z_h

$\langle z_h \rangle$	$A_{\cos \phi_h}$	$\sigma_{A_{\cos \phi_h}}$	$A_{\cos 2\phi_h}$	$\sigma_{A_{\cos 2\phi_h}}$
0.061	-0.0196	0.0013	-0.0189	0.0029
0.12	-0.0403	0.0017	-0.0147	0.0036
0.16	-0.0352	0.0027	-0.0024	0.0056
0.19	-0.0367	0.0029	-0.0053	0.0060
0.21	-0.0279	0.0032	0.0170	0.0065
0.24	-0.0219	0.0035	0.0106	0.0070
0.26	-0.0303	0.0038	0.0309	0.0075
0.29	-0.0170	0.0041	0.0302	0.0082
0.32	-0.0254	0.0036	0.0190	0.0071
0.37	-0.0224	0.0035	0.0396	0.0068
0.44	-0.0288	0.0035	0.0496	0.0069
0.55	-0.0491	0.0039	0.0582	0.0076
0.72	-0.0948	0.0050	0.0247	0.0100

Table A.11: results for the all hadron sample, positive hadrons, binned in P_t^h

$\langle z_h \rangle$	$A_{\cos \phi_h}$	$\sigma_{A_{\cos \phi_h}}$	$A_{\cos 2\phi_h}$	$\sigma_{A_{\cos 2\phi_h}}$
0.15	-0.0444	0.0015	-0.0205	0.0032
0.24	-0.0448	0.0018	-0.0294	0.0037
0.30	-0.0411	0.0020	-0.0200	0.0041
0.36	-0.0410	0.0021	-0.0139	0.0044
0.42	-0.0387	0.0021	-0.0058	0.0045
0.50	-0.0371	0.0022	0.0034	0.0045
0.59	-0.0465	0.0026	0.0122	0.0054
0.70	-0.0514	0.0028	0.0352	0.0057
0.87	-0.0672	0.0031	0.0144	0.0065
1.24	-0.0835	0.0047	0.0623	0.0097

Table A.12: results for the all hadron sample, negative hadrons, binned in P_t^h

$\langle P_t^h \rangle [GeV]$	$A_{\cos \phi_h}$	$\sigma_{A_{\cos \phi_h}}$	$A_{\cos 2\phi_h}$	$\sigma_{A_{\cos 2\phi_h}}$
0.15	-0.0187	0.0017	-0.0139	0.0035
0.24	-0.0229	0.0019	-0.0270	0.0040
0.30	-0.0199	0.0021	-0.0101	0.0045
0.36	-0.0205	0.0023	-0.0033	0.0047
0.42	-0.0199	0.0023	0.0136	0.0048
0.50	-0.0202	0.0023	0.0133	0.0049
0.59	-0.0303	0.0028	0.0346	0.0059
0.70	-0.0353	0.0030	0.0469	0.0062
0.87	-0.0577	0.0035	0.0674	0.0071
1.24	-0.0708	0.0051	0.0766	0.0105

Table A.13: results for the leading hadron sample, positive hadrons, binned in x

$\langle x \rangle$	$A_{\cos \phi_h}$	$\sigma_{A_{\cos \phi_h}}$	$A_{\cos 2\phi_h}$	$\sigma_{A_{\cos 2\phi_h}}$
0.0067	0.0137	0.0152	0.0358	0.0283
0.011	0.0083	0.0062	0.0308	0.0104
0.017	-0.0248	0.0049	0.0301	0.00864
0.024	-0.0645	0.0043	0.0024	0.00835
0.031	-0.0784	0.0034	-0.0348	0.00684
0.042	-0.0735	0.0036	-0.0364	0.0071
0.063	-0.0614	0.0035	-0.0427	0.00712
0.14	-0.0297	0.0035	-0.0003	0.00694

Table A.14: results for the leading hadron sample, negative hadrons, binned in x

$\langle x \rangle$	$A_{\cos \phi_h}$	$\sigma_{A_{\cos \phi_h}}$	$A_{\cos 2\phi_h}$	$\sigma_{A_{\cos 2\phi_h}}$
0.0067	0.0207	0.0155	-0.0083	0.03
0.011	0.0197	0.0069	0.0865	0.0113
0.017	-0.0351	0.0053	0.0721	0.0094
0.023	-0.0610	0.0049	0.0321	0.0093
0.031	-0.0693	0.0039	0.0103	0.0077
0.042	-0.0515	0.0042	0.0062	0.0083
0.063	-0.0382	0.0044	0.0119	0.0086
0.14	0.0170	0.0044	0.0142	0.0099

Table A.15: results for the leading hadron sample, positive hadrons, binned in Q^2

$\langle Q^2 \rangle [\text{GeV}^2]$	$A_{\cos \phi_h}$	$\sigma_{A_{\cos \phi_h}}$	$A_{\cos 2\phi_h}$	$\sigma_{A_{\cos 2\phi_h}}$
1.12	-0.046	0.0035	-0.0104	0.0068
1.41	-0.060	0.0034	-0.0063	0.0069
1.79	-0.0549	0.0039	-0.0163	0.0078
2.34	-0.0745	0.0036	-0.0368	0.0074
3.22	-0.0660	0.0042	-0.0276	0.0086
4.77	-0.0469	0.0040	-0.0170	0.0082
7.62	-0.0386	0.0046	0.0019	0.0094
18.0	-0.0549	0.0058	0.0334	0.0122

Table A.16: results for the leading hadron sample, negative hadrons, binned in Q^2

$\langle Q^2 \rangle [\text{GeV}^2]$	$A_{\cos \phi_h}$	$\sigma_{A_{\cos \phi_h}}$	$A_{\cos 2\phi_h}$	$\sigma_{A_{\cos 2\phi_h}}$
1.12	-0.0381	0.0040	0.0447	0.00766
1.41	-0.0494	0.0039	0.04	0.0077
1.79	-0.0497	0.0045	0.0047	0.0088
2.34	-0.0554	0.0043	0.0259	0.0084
3.22	-0.039	0.0051	0.0411	0.0100
4.76	-0.019	0.0049	0.0141	0.0098
7.59	0.0025	0.0058	0.0591	0.0116
17.6	-0.010	0.0076	0.049	0.0161

Table A.17: results for the leading hadron sample, positive hadrons, binned in y

$\langle y \rangle$	$A_{\cos \phi_h}$	$\sigma_{A_{\cos \phi_h}}$	$A_{\cos 2\phi_h}$	$\sigma_{A_{\cos 2\phi_h}}$
0.12	-0.0210	0.0044	-0.0290	0.00816
0.15	-0.0440	0.0034	-0.0260	0.00663
0.19	-0.0620	0.0032	-0.0169	0.00632
0.24	-0.0567	0.0037	-0.0182	0.00728
0.30	-0.0482	0.0042	0.000	0.00792
0.36	-0.0286	0.0055	0.034	0.0099
0.42	-0.0302	0.0071	-0.0029	0.0126
0.49	-0.0253	0.0087	0.0245	0.015
0.58	-0.0312	0.0111	-0.0039	0.0198
0.71	-0.0017	0.0166	0.0164	0.0318

Table A.18: results for the leading hadron sample, negative hadrons, binned in y

$\langle y \rangle$	$A_{\cos \phi_h}$	$\sigma_{A_{\cos \phi_h}}$	$A_{\cos 2\phi_h}$	$\sigma_{A_{\cos 2\phi_h}}$
0.12	0.0110	0.0054	0.0223	0.0101
0.15	-0.0252	0.0040	0.0127	0.0078
0.19	-0.0442	0.0037	0.0186	0.0074
0.24	-0.0482	0.0044	0.0361	0.0084
0.30	-0.0374	0.0049	0.0615	0.0090
0.36	-0.0151	0.0065	0.0570	0.0113
0.42	-0.0302	0.0084	0.0566	0.0145
0.49	0.0002	0.0097	0.0459	0.0164
0.58	0.0235	0.0136	0.0657	0.0226
0.71	-0.0001	0.0170	0.0311	0.0336

Table A.19: results for the leading hadron sample, positive hadrons, binned in z_h

$\langle z_h \rangle$	$A_{\cos \phi_h}$	$\sigma_{A_{\cos \phi_h}}$	$A_{\cos 2\phi_h}$	$\sigma_{A_{\cos 2\phi_h}}$
0.28	-0.0339	0.0035	-0.0089	0.0072
0.32	-0.0348	0.0039	-0.0091	0.0080
0.36	-0.0427	0.0041	-0.0011	0.0082
0.40	-0.0419	0.0043	-0.0110	0.0086
0.45	-0.0536	0.0036	-0.0046	0.0072
0.55	-0.0670	0.0031	0.0012	0.0063
0.72	-0.0950	0.0038	-0.0624	0.0077

Table A.20: results for the leading hadron sample, negative hadrons, binned in z_h

$\langle z_h \rangle$	$A_{\cos \phi_h}$	$\sigma_{A_{\cos \phi_h}}$	$A_{\cos 2\phi_h}$	$\sigma_{A_{\cos 2\phi_h}}$
0.28	-0.0165	0.0039	0.0342	0.0078
0.32	-0.0255	0.0044	0.0077	0.0088
0.36	-0.0255	0.0047	0.0404	0.0092
0.41	-0.0148	0.0051	0.0592	0.0099
0.45	-0.0332	0.0043	0.0425	0.0083
0.55	-0.0496	0.0039	0.0568	0.0076
0.72	-0.0954	0.0050	0.025	0.010

Table A.21: results for the leading hadron sample, positive hadrons, binned in P_t^h

$\langle z_h \rangle$	$A_{\cos \phi_h}$	$\sigma_{A_{\cos \phi_h}}$	$A_{\cos 2\phi_h}$	$\sigma_{A_{\cos 2\phi_h}}$
0.16	-0.0341	0.0043	-0.0160	0.0087
0.24	-0.0518	0.0044	-0.0398	0.0089
0.30	-0.0512	0.0046	-0.0233	0.0093
0.36	-0.0608	0.0046	-0.0142	0.0092
0.43	-0.0528	0.0044	-0.0322	0.0086
0.50	-0.0578	0.0041	-0.0129	0.0081
0.59	-0.0592	0.0044	-0.0260	0.0088
0.70	-0.0607	0.0043	0.0096	0.0085
0.87	-0.0866	0.0042	-0.0040	0.0087
1.27	-0.0941	0.0055	0.0367	0.0114

Table A.22: results for the leading hadron sample, negative hadrons, binned in P_t^h

$\langle P_t^h \rangle [GeV]$	$A_{\cos \phi_h}$	$\sigma_{A_{\cos \phi_h}}$	$A_{\cos 2\phi_h}$	$\sigma_{A_{\cos 2\phi_h}}$
0.16	-0.0216	0.0050	0.0176	0.0099
0.24	-0.0322	0.0052	0.0051	0.0103
0.30	-0.0468	0.0054	-0.0008	0.0107
0.36	-0.0286	0.0057	0.0527	0.0107
0.43	-0.0367	0.0053	0.0300	0.0103
0.50	-0.0342	0.0048	0.0259	0.0094
0.59	-0.0354	0.0053	0.0422	0.0104
0.70	-0.0452	0.0050	0.0424	0.00988
0.87	-0.0641	0.0050	0.0600	0.0101
1.27	-0.0779	0.0064	0.068	0.013

Bibliography

- [1] D. J. Gross and F. A. Wilczek. *Ultraviolet Behavior of Non-Abelian Gauge Theories*. Phys. Rev. Lett. **30** (1973) 1343.
- [2] H.D. Politzer. *Reliable Perturbative Results for Strong Interactions?* Phys. Rev. Lett. **30** (1973) 1346.
- [3] European Muon Collaboration. *A Measurement of the Spin Asymmetry and Determination of the Structure Function g_1 in deep inelastic Muon-Proton Scattering*. Phys. Lett. **B206** (1988) 364.
- [4] H. Georgi and H. D. Politzer. *Clean Tests of Quantum Chromodynamics in μp Scattering*. Phys. Rev. Lett. **40** (1978) 3-6.
- [5] R. N. Cahn. *Azimuthal dependence in leptonproduction: A simple parton model calculation*. Phys. Lett. **B78** (1978) 269-273.
- [6] V. Barone and P. Ratcliffe. *Transverse Spin Physics*. World Scientific Publishing Co. Pte. Ltd (2003).
- [7] European Muon Collaboration. *Measurement of hadronic azimuthal distributions in deep inelastic muon proton scattering*. Phys. Lett. **B130** (1983) 118.
- [8] European Muon Collaboration. *Measurement of hadronic azimuthal distributions in deep inelastic muon proton scattering*. Z. Phys. **C34** (1987), 277.
- [9] Fermilab E665 Collaboration. *Perturbative QCD effects observed in 490 GeV deep-inelastic muon scattering*. Phys. Rev. **D48** (1993), 5057–5066.
- [10] ZEUS Collaboration. *Measurement of Azimuthal Asymmetries in Deep Inelastic Scattering*. Phys.Lett. **B481** (2000) 199-212, [hep-ex/0003017v2].
- [11] I. Ludwig. *Azimuthal Asymmetries and the Cahn Effect at COMPASS*. Diploma thesis (2004).
- [12] G. Sbrizzai. *Simulazione di Eventi SIDIS in GRID per l'esperimento COMPASS*. Diploma thesis (2007), in Italian.
- [13] W. Greiner et al. *Quantum Chromodynamics*. Springer-Verlag, 2002.

-
- [14] A. Bacchetta et al. *Semi-inclusive deep inelastic scattering at small transverse momentum*. JHEP **02** (2007) 93, [hep-ph/0611265].
- [15] X. Ji et al. *QCD Factorization for Semi-Inclusive Deep-Inelastic Scattering at Low Transverse Momentum*. Phys. Rev. **D71** (2005) 034005 [hep-ph/0404183].
- [16] A. König and P. Kroll. *A realistic calculation of the azimuthal asymmetry in semi-inclusive deep inelastic scattering*. Z.Phys. **C16**(1982) 89-92.
- [17] M. Anselmino et al. *The role of Cahn and Sivers effects in Deep Inelastic Scattering*. Phys. Rev. **D71** (2005) 074006 [hep-ph/0501196 v2].
- [18] A. Kotzinian. *New Quark Distributions and Semi-Inclusive Electroproduction on Polarized Nucleons*. Nucl. Phys. **B441**(1995) 234.
- [19] P. J. Mulders and R. D. Tangerman. *The complete tree-level result up to order $1/Q$ for polarized deep-inelastic lepton production*. Nucl.Phys. **B461** (1996) 197-237 [hep-ph/9510301].
- [20] HERMES Collaboration. *Evidence for a Single-Spin Azimuthal Asymmetry in Semi-inclusive Pion Electroproduction*. Phys. Rev. Lett. **84** (2000) 4047-4051.
- [21] COMPASS Collaboration. *A new measurement of the Collins and Sivers asymmetries on a transversely polarised deuteron target*. Nucl. Phys. **B765** (2007) 31-70, [hep-ex/0610068].
- [22] Belle collaboration. *Measurement of azimuthal asymmetries in inclusive production of hadron pairs in e^+e^- annihilation at Belle*. Phys. Rev. Lett. **96** (2006) 232002, [hep-ex/0507063].
- [23] V. Barone et al. *On the $\cos 2\phi$ asymmetry in unpolarized lepton production*. Phys. Lett **B632** (2006) 277-281.
- [24] V. Barone et al. *A systematic phenomenological study of the $\cos 2\phi$ asymmetry in unpolarized semi-inclusive DIS*. to be published (2008).
- [25] J. Chay, S. D. Ellis, and W. J. Stirling. *Azimuthal asymmetry in lepton-proton scattering at high energies*. Phys. Rev. **D45** (1992) 46-54.
- [26] A. Daleo, D. de Florian, and R. Sassot. *$\mathcal{O}(\alpha_s^2)$ QCD corrections to the electroproduction of hadrons with high transverse momentum*. Phys. Rev. **D71** (2005) 034013.
- [27] A. Mendez. *QCD predictions for semi-inclusive and inclusive lepton production*. Nucl. Phys. **B145** (1978) 199-220.
- [28] COMPASS Collaboration. *The COMPASS Experiment at CERN*. Nucl. Instr. Meth. **A577** 455, [hep-ex/0703049].
- [29] N. Doble et al. *The upgraded muon beam at the SPS*. Nucl. Instr. Meth. **A343** (1994) 351.

- [30] SMC Collaboration. *The Polarized Double Cell Target of the SMC*. Nucl. Instr. Meth. **A437** (1999) 23.
- [31] C. Bernet et al. *The COMPASS trigger system for muon scattering*. NIM **A550** (2005) 217-240.
- [32] H. Fischer et al. *The COMPASS Data Acquisition System*. IEEE Trans. Nucl. Sci. **49** (2002) 443.
- [33] CERN. *CASTOR web page*. <http://castor.web.cern.ch/castor/>.
- [34] B. Gobbo. *coral web page*. <http://coral.web.cern.ch/coral/>.
- [35] R. Brun et al. *Root Users Guide 5.17*. <http://root.cern.ch/>.
- [36] R. Frühwirth et al. *Data Analysis Techniques for High-Energy Physics*. Cambridge University Press, 2000.
- [37] Y. Bedfer et al. *COMPASS's track reconstruction algorithm*. January 2004, COMPASS-note 2004-01.
- [38] V. Alexakhin et al. *Vertex reconstruction in the COMPASS spectrometer. Part I. Monte Carlo studies*. December 2001, COMPASS-note 2001-17.
- [39] S. Gerassimov. *PHAST web page*. <http://ges.home.cern.ch/ges/phast/>.
- [40] G. Ingelman, A. Edin, and J. Rathsmann. *LEPTO 6.5 A Monte - Carlo generator for Deep Inelastic Lepton Nucleon Scattering*.
- [41] V. Alexakhin. *COMgeant web page*. <http://valexakh.web.cern.ch/valexakh/wwwcomg/index.html>.
- [42] CERN-IT division. *Geant web page*. <http://wwwasd.web.cern.ch/wwwasd/geant/index.html>.
- [43] COMPASS Collaboration. *The deuteron spin-dependent structure function $g_1(d)$ and its first moment*. Phys. Lett. **B647** (2007) 8-17 [hep-ex/0609038].
- [44] D. Neyret. *COMPASS Online Logbook*. <http://wwwcompass.cern.ch/runLogbook/dirphp/>. e.g. comment # 8986, 9237, 10571.
- [45] C. Schill. *Period Coordinator Report 28.05.04 - 04.06.04*. http://wwwcompass.cern.ch/compass/run2004/reports/week_04_23.ps.
- [46] S. Koblitz et al. *COMPASS STABILITY PAGE*. <http://wwwcompass.cern.ch/compass/software/offline/input/stab/index.html>.
- [47] A. Bressan. *Origin and cure of the peak in y* . April 2007, COMPASS-note 2006-13.
- [48] P. Schiavon. *Particle identification in COMPASS RICH-1, Progress Report*. September 2001, COMPASS-note 2001-12.
- [49] P. Schiavon. *Hints for PID in RICH-1*. May 2003, COMPASS-note 2003-02.

-
- [50] T. Sjostrand et al. *PYTHIA 6.3, Physics and Manual*, 2003. [hep-ph/0308153].
- [51] M. Burkardt. *Transverse deformation of parton distributions and transversity decomposition of angular momentum*. Phys. Rev. **D72**,(2005), 094020.
- [52] M. Göckeler et al. *Transverse spin structure of the nucleon from lattice QCD simulations*. Phys. Rev. Lett. **98** (2007) 222001, [hep-lat/0612032].
- [53] D. Sivers. *Single-spin production asymmetries from the hard scattering of pointlike constituents*. Phys. Rev. **D41** (1990),83-90.
- [54] M. Anselmino et al. *Extracting the Sivers function from polarized semi-inclusive deep inelastic scattering data and making predictions*. Phys. Rev. **D72** (2005) 094007.
- [55] M. Anselmino et al. *Transversity and Collins functions from SIDIS and e^+e^- data*. Phys. Rev. **D75** (2007) 054032, [hep-ph/0701006].
- [56] H. Fischer. *Private communication*. Feb 2008.
- [57] CLAS Collaboration: H. Avakian. *Measurement of Beam-Spin Asymmetries for Deep Inelastic π^+ Electroproduction*. Phys. Rev. **D69** (2004) 112-4, [hep-ex/0301005].
- [58] J. Cham. *phdcomics*. <http://www.phdcomics.com/>.
- [59] V. Gates, E. Kangaroo, M. Roachcock, and W. C. Gall. *STUPERSPACE*. Physica **15D** (1985)289-293.

Acknowledgments

As usual, this thesis would not have been possible without the support of many people. In particular, I'd like to thank:

- Prof. Kay Königsmann for the opportunity to join the Freiburg group to write this thesis.
- Prof. Horst Fischer for excellent supervision and many helpful comments and suggestions.
- My test readers: Jochen Barwind, Andreas Mutter, Frank Nerling, Christian Schill, Anselm Vossen and in particular Heiner Wollny, who had the dubious pleasure to get always the first more or less readable version, for many helpful comments and corrections for this thesis. All remaining mistakes are of course my responsibility.
- Frank Nerling, Giulio Sbrizzai, Donghee Kang, Jochen Barwind, Jasmin Kiefer, Anselm Vossen, Heiner Wollny for many fruitful discussions.
- Roland Hagemann and Andreas Mutter for many helpful LINUX tips.
- All members of the Freiburg group for the friendly and productive atmosphere.
- Jasmin Kiefer for the introduction to the mysterious world of PHAST and ROOT.
- my family and friends for constant support.
- Anselm Vossen for introducing me to the wonderful world of [58]
- V. Gates, E.Kangaroo, M.Roachcock, W.C.Gall for the discovery of Stuperspace [59]
- Everyone who feels he should be acknowledged and I forgot to mention

B. Deutschsprachige Zusammenfassung

Azimutale Asymmetrien in unpolarisierter Lepton-Nukleon-Streuung wurden ursprünglich Ende der 70er Jahre als Test der Quantenchromodynamik vorgeschlagen, da die QED in führender Ordnung keinerlei Modulation des Wirkungsquerschnitts vom Azimutalwinkel des Hadrons ϕ_h vorhersagt. Die QCD sagt bereits in führender Ordnung eine $\cos \phi_h$ und $\cos 2\phi_h$ Modulation voraus. Der Winkel ϕ_h wird dabei um die Richtung des virtuellen Photons gemessen. Kurz darauf wies R. Cahn jedoch darauf hin, dass es auch in führender Ordnung QED möglich ist, solche azimutalen Modulationen zu erzeugen, falls Quarks eine Impulskomponente transversal zur Bewegungsrichtung des Photon-Nukleon Systems haben. Um Quarkmassen vernachlässigen zu können erfolgt die theoretische Beschreibung der Lepton-Nukleon-Streuung meist in einem Bezugssystem, in welchem das Nukleon kollinear zum Photon und stark relativistisch ist. Daher wird dieser Transversalimpuls häufig vernachlässigt. Ein zusätzlicher Effekt (Boer-Mulders-Effekt) kommt durch einen Beitrag der k_t -abhängigen Parton Verteilungsfunktion h_1^\perp zustande. Diese beschreibt die Verteilung transversal polarisierter Quarks im unpolarisierten Nukleon.

Im Rahmen dieser Diplomarbeit wurden die $\cos \phi_h$ - und die $\cos 2\phi_h$ -Momente des semi-inklusiven Wirkungsquerschnittes aus Daten, die 2004 am COMPASS-Experiment genommen wurden, bestimmt. Da das COMPASS Experiment einen polarisierten Muonstrahl verwendet, tritt zusätzlich eine $\sin \phi_h$ -Abhängigkeit auf, die ebenfalls gemessen wurde. Da die Größe der Modulationen von verschiedenen, für den Streuprozess charakteristischen Größen abhängt, wurden die Momente als Funktion dieser Variablen x, y, Q^2, z_h und P_t^h bestimmt. Zusätzlich wurde die Analyse für sogenannte führende Hadronen durchgeführt. Diese haben eine erhöhte Wahrscheinlichkeit das gestreute Quark zu enthalten, und sollten daher den Cahn Effekt besonders deutlich zeigen. Die QCD beeinflusst alle Hadronen, daher wurde die Analyse ebenfalls ohne diese Auswahl durchgeführt.

Die größte Herausforderung der Analyse besteht darin, dass auch durch unterschiedliche geometrische Akzeptanz des Detektors solche Abhängigkeiten verursacht werden. Diese Effekte wurden mit Hilfe einer MC Simulation untersucht und die Daten damit korrigiert. Um die Korrektur zu testen, wurden verschiedene Tests durchgeführt. Diese beruhen meist darauf, die Ergebnisse, die man erhält, wenn man nur Ereignisse aus einem Teil des Targets berücksichtigt mit den Resultaten für einen anderen Teils des Targets zu vergleichen. Auch wenn diese Tests Anzeichen für systematische Fehler zeigen, sind sie doch gut genug, um der Akzeptanzkorrektur im Prinzip zu vertrauen. Für die präzise Bestimmung eines systematischen Fehlers sind aber noch weitere Studien nötig.

Die erhaltenen Ergebnisse wurden verwendet, um mit einem vereinfachten Modell den mittleren Transversalimpuls der Quarks k_t abzuschätzen. Es ergab sich ein Wert von $\langle k_t^2 \rangle \approx 0.1 \text{ GeV}^2$. Das verwendete Modell, welches nur den Cahn Effekt berücksichtigt, erwies sich jedoch als unzureichend, um alle beobachteten kinematischen Abhängigkeiten bei den führenden Hadronen zu erklären. Trotzdem liegt dieser Wert in der erwarteten Größenordnung, aber verfeinerte Modelle, die auch die anderen Beiträge berücksichtigen, sollten es ermöglichen, einen genaueren Wert anzugeben. Die erhaltenen $\cos 2\phi_h$ -Momente wurden mit einer kürzlich angefertigten Modellrechnung verglichen, die sowohl den Cahn Effekt als auch Boer-Mulders und QCD Beiträge berücksichtigt. Allerdings beruht die Vorhersage für den Boer-Mulders-Effekt auf relativ starken Annahmen, da h_1^\perp noch nicht gemessen werden konnte. Trotzdem ist die Übereinstimmung ermutigend und sollte es ermöglichen, das Modell zu verfeinern.

Erklärung

Diese Arbeit ist von mir selbständig verfasst worden und ich habe keine anderen als die angegebenen Quellen als Hilfsmittel verwendet.

Wolfgang Käfer, Februar 2008